1996-12

Unbalanced frontogenesis with constant potential vorticity

Neves, Alberto P. C.

Monterey, California. Naval Postgraduate School

NAVAL POSTGRADUATE SCHOOL
Monterey, California

THESIS

UNBALANCED FRONTOGENESIS WITH CONSTANT POTENTIAL VORTICITY

by

Alberto P. C. Neves

December, 1996

Thesis Co-Advisors: R. T. Williams
M. S. Peng

Approved for public release; distribution is unlimited.

REPORT DOCUMENTATION PAGE

Form Approved OMB No. 0704-0188

1. AGENCY USE ONLY *(Leave blank)*	2. REPORT DATE December 1996	3. REPORT TYPE AND DATES COVERED Master's Thesis

4. TITLE AND SUBTITLE UNBALANCED FRONTOGENESIS WITH CONSTANT POTENTIAL VORTICITY

5. FUNDING NUMBERS

6. AUTHOR(S) Neves, Alberto P. C.

7. PERFORMING ORGANIZATION NAME(S) AND ADDRESS(ES)
Naval Postgraduate School
Monterey CA 93943-5000

8. PERFORMING ORGANIZATION REPORT NUMBER

9. SPONSORING/MONITORING AGENCY NAME(S) AND ADDRESS(ES)

10. SPONSORING/MONITORING AGENCY REPORT NUMBER

11. SUPPLEMENTARY NOTES The views expressed in this thesis are those of the author and do not reflect the official policy or position of the Department of Defense or the U.S. Government.

12a. DISTRIBUTION/AVAILABILITY STATEMENT
Approved for public release; distribution is unlimited.

12b. DISTRIBUTION CODE

13. ABSTRACT *(maximum 200 words)*

The numerical model of Williams et al. (1992) is used to study frontogenesis from unbalanced initial conditions. The dependent variables are assumed to be independent of y. The hydrostatic Boussinesq primitive equations are used with no diffusion of heat or momentum. The model is bounded at the top and bottom by rigid planes. Periodic boundary conditions are used in the horizontal. The lateral boundaries are placed far enough from the imbalance region to avoid wave reflection. The atmosphere is assumed to have constant vertical temperature stratification.

The initial imbalance is obtained by allowing a horizontal temperature gradient to exist while the initial wind is zero. In a stably stratified atmosphere, gravity waves are excited and propagate away from the imbalance region, provided no reflection occurs in the lateral boundaries. Therefore, the atmosphere tends toward a geostrophic balance away from vertical boundaries. Near these boundaries, the temperature gradient oscillates or it collapses into a front, depending on the initial Rossby (Ro) and Froude (F) numbers. A relationship between Ro and F is established which separates situations where a front may or may not form. Numerical solutions show the formation of a front within a finite period of time that tilts toward the cold air.

14. SUBJECT TERMS *Type the keywords (at least three) for your thesis in over these words; all keywords must be unclassified.

15. NUMBER OF PAGES 88

16. PRICE CODE

17. SECURITY CLASSIFICATION OF REPORT	18. SECURITY CLASSIFICATION OF THIS PAGE	19. SECURITY CLASSIFICATION OF ABSTRACT	20. LIMITATION OF ABSTRACT
Unclassified	Unclassified	Unclassified	UL

NSN 7540-01-280-5500

Standard Form 298 (Rev. 2-89)
Prescribed by ANSI Std. 239-18 298-102

Approved for public release; distribution is unlimited.

UNBALANCED FRONTOGENESIS WITH CONSTANT POTENTIAL VORTICITY

Alberto P. C. Neves
Lieutenant Commander, Brazilian Navy
B.S., Brazilian Naval Academy, 1984

Submitted in partial fulfillment
of the requirements for the degree of

MASTER OF SCIENCE IN METEOROLOGY AND PHYSICAL OCEANOGRAPHY

from the

NAVAL POSTGRADUATE SCHOOL
December 1996

Author: [redacted]

Alberto P. C. Neves

Approved by: [redacted]

Roger T. Williams, Thesis Co-Advisor

[redacted]

Melinda S. Peng, Thesis Co-Advisor

[redacted]

Carlyle H. Wash, Chairman
Department of Meteorology

ABSTRACT

The numerical model of Williams et al. (1992) is used to study frontogenesis from unbalanced initial conditions. The dependent variables are assumed to be independent of y. The hydrostatic Boussinesq primitive equations are used with no diffusion of heat or momentum. The model is bounded at the top and bottom by rigid planes. Periodic boundary conditions are used in the horizontal. The lateral boundaries are placed far enough from the imbalance region to avoid wave reflection. The atmosphere is assumed to have constant vertical temperature stratification.

The initial imbalance is obtained by allowing a horizontal temperature gradient to exist while the initial wind is zero. In a stably stratified atmosphere, gravity waves are excited and propagate away from the imbalance region, provided no reflection occurs in the lateral boundaries. Therefore, the atmosphere tends toward a geostrophic balance away from vertical boundaries. Near these boundaries, the temperature gradient oscillates or it collapses into a front, depending on the initial Rossby (Ro) and Froude (F) numbers. A relationship between Ro and F is established which separates situations where a front may or may not form. Numerical solutions show the formation of a front within a finite period of time that tilts toward the cold air.

TABLE OF CONTENTS

ACKNOWLEDGMENT

This thesis research represents more than the final product of the work done in the past several months. It is the sum of effort and commitment combining more than two years of courses, homework, readings, and laboratories. The size of this enterprise is much bigger than the labor of one person. This study was possible due to the involvement of numerous people, who directly and indirectly helped to transform it into reality.

My first words of appreciation go to my wife, Neide, whose love and patience were the main support during this long period. Her dedication and assistance were crucial for the success of this study. Especially important was the presence of my daughter Carolina, whose smile gave me great joy in difficult times. To my parents, Lourdes and Alberto, I offer a special thanks. Their presence and guidance throughout my life has been monumental.

To my mentor, Prof. R. T. Williams, my special thanks for the assistance and patience. His unparalleled dedication and expertise made it possible for me to understand very difficult concepts and ideas, both during the thesis research and the numerous hours of classroom instruction. With always precise orientation, he paved the way for this intense and difficult study. Thanks to Prof. M. S. Peng for helping me with the model preparation and thesis revision.

I would also like to thank all the faculty and support personnel in the

Meteorology and Oceanography curricular office, in the Meteorology and Oceanography Departments, and in the International Office. Their help and attention were very important in all stages of this work.

Finally, my very special thanks to the Brazilian Navy for giving me the opportunity to be here and improve my professional life. The Navy's investment will certainly pay great dividends in all future assignments.

I. INTRODUCTION

Frontogenesis can be described as the process of formation of small-scale motion field from an initial larger scale state. Baroclinic instability is the main source of disturbance energy, that can eventually produce the energy cascade from the large to the small scale atmospheric states (Williams 1967; Hoskins and Bretherton 1972). Many different mechanisms can work to produce or modify a front. Numerical experiments (Williams et al. 1992) show the weakening of a front approaching a topographic ridge and reintensifying as it goes downslope. Turbulent horizontal and vertical diffusion can play an important role in opposing frontogenetical effects and in modifying the frontal structure (Williams 1974; Keyser and Anthes 1982). Background shearing or stretching deformation wind fields can generate large temperature gradients and are equally important in frontogenetical processes (Stone 1966; Hoskins and Bretherton 1972). Differential heating can be either frontogenetical or frontolytic, depending on whether it enhances or weakens the temperature gradient.

Balanced frontogenesis has mass and momentum fields in near thermal wind balance and relative vorticity is larger than horizontal divergence. Williams (1972) used balanced initial conditions to show frontal formation with linear and nonlinear primitive equation models. The latter is more realistic in the sense that a discontinuity occurs within a finite period of time and the front tilts toward the cold air. This is due to the temperature advection by the divergent part of the wind, not present on the linear case. Hoskins and Bretherton (1972) suggest that relative vorticity will remain larger than

horizontal divergence during this process, in the absence of friction, even when the Rossby number is greater than one.

The frontogenesis is unbalanced when the mass and momentum fields are not in semi-geostrophic balance. This situation is usually associated with large near-surface differential heating. A large temperature gradient can cause a non-geostrophic horizontal pressure gradient that can lead to frontal formation. The imbalance can originate in strong baroclinic zones associated with the sea-breeze circulation and in regions where partial cloud cover can cause large temperature gradients. Clear skies ahead of and extensive cloudiness behind a cold front can produce an imbalance during the morning heating. This imbalance can lead to a stronger front than the balanced one, which is forced by the large-scale flow.

Blumen and Williams (1996, hereafter BW96) investigate unbalanced frontogenesis for a zero potential vorticity case. In one of their initial conditions, the temperature has an error function distribution and the fluid is at rest. A heat source can be considered to generate the imbalance but no source exists after the initial time. The equations use the Boussinesq approximation and friction is neglected during the process of frontal formation. They find an inertial oscillation in the horizontal velocity components, and frontogenesis when the Rossby number is sufficiently large.

The purpose of this study is to extend the work of BW96 for the case of a non-zero constant potential vorticity, with similar initial conditions. When the atmosphere is vertically stratified, gravity waves are allowed to propagate away from the initial imbalance and the frontogenesis process can be significantly modified. The main

objective of this research is to determine a curve in Rossby number - Froude number space which separates frontogenesis from non-frontogenesis cases. Various analyses and displays will be used in order to determine whether a frontal discontinuity has formed. The boundary conditions are the same as used by BW96, and heat sources and friction are neglected. Williams and Kurth (1976) also considered this problem, but with different initial conditions.

II. MODEL FORMULATION

A. BASIC EQUATIONS

The study of surface frontogenesis in this work involves just the lower portion of the troposphere where the density variation is small. To simplify the problem of modeling the frontal formation, the atmosphere will be considered incompressible, inviscid, and in hydrostatic balance. The equations developed here follow Williams et al. (1992) adapted to a flat topography. The vertical axis is normalized with the height of the upper boundary, H, and defined as

$$\zeta = \frac{z}{H} \tag{1}$$

Using equation (1) to transform the Boussinesq equations (Ogura and Phillips 1962) we get

$$\frac{\partial \mathbf{V}}{\partial t} + \mathbf{V}.\nabla\mathbf{V} + \dot{\zeta}\frac{\partial \mathbf{V}}{\partial \zeta} = -\nabla\phi - f\mathbf{k}\times\mathbf{V} + \mathbf{F}, \tag{2}$$

$$\frac{\partial \theta}{\partial t} + \mathbf{V}.\nabla\theta + \dot{\zeta}\frac{\partial \theta}{\partial \zeta} = Q, \tag{3}$$

$$\nabla.\mathbf{V} + \frac{\partial \dot{\zeta}}{\partial \zeta} = 0, \tag{4}$$

$$\frac{\partial \phi}{\partial \zeta} = \frac{g}{\theta_0} H\theta, \tag{5}$$

where

$$\theta = T(p_0 / p)^{\kappa} - \theta_0,$$

$$\phi = \theta_0[c_p(p_0 / p)^{\kappa} + gz / \theta_0 - c_p].$$

Friction is neglected and Q represents dry convective adjustment. The quantities p_0 and θ_0 are constant and the other symbols have their usual meteorological meaning.

No along-front variation will be considered here and the two-dimensional domain is established in the x-ζ plane. The domain is bounded by two horizontal rigid plates and periodic boundary conditions are used in x. The top and bottom boundary conditions are

$$\dot{\zeta} = 0 \quad \text{at} \quad \zeta = 0,\ 1, \tag{6}$$

and the dependent variables are

$$\mathbf{V} = u(x, \zeta, t)\mathbf{i} + v(x, \zeta, t)\mathbf{j}, \tag{7a}$$

$$\dot{\zeta} = \dot{\zeta}(x, \zeta, t), \tag{7b}$$

$$\theta = \theta(x, \zeta, t), \tag{7c}$$

$$\phi = \phi(x, \zeta, t). \tag{7d}$$

Using the variables in (7) and the condition $\partial/\partial y = 0$, the system (2) - (5) becomes, in flux form

$$\frac{\partial u}{\partial t}+\frac{\partial uu}{\partial x}+\frac{\partial u\dot{\zeta}}{\partial \zeta}+\frac{\partial \phi}{\partial x}-fv=0, \tag{8}$$

$$\frac{\partial v}{\partial t}+\frac{\partial uv}{\partial x}+\frac{\partial v\dot{\zeta}}{\partial \zeta}+fu=0, \tag{9}$$

$$\frac{\partial \theta}{\partial t}+\frac{\partial u\theta}{\partial x}+\frac{\partial \theta\dot{\zeta}}{\partial \zeta}-Q=0, \tag{10}$$

$$\frac{\partial u}{\partial x}+\frac{\partial \dot{\zeta}}{\partial \zeta}=0, \tag{11}$$

$$\frac{\partial \phi}{\partial \zeta}=\frac{g}{\theta_0}H\theta. \tag{12}$$

The hydrostatic equation (12) can be vertically integrated and solved for ϕ:

$$\phi=\phi_0+\phi_s, \tag{13}$$

where

$$\phi_s=\int_0^{\zeta}\frac{g}{\theta_0}H\theta\, d\zeta,$$

and ϕ_0 is the value at the lower boundary. The variable ϕ cannot be determined from the hydrostatic equation because of the rigid upper boundary, since ϕ is not known at any level. To fix this problem, a dynamic condition is obtained from the continuity

equation. Vertically integrating (11) from $\zeta = 0$ to $\zeta = 1$ and using (6) yields

$$\frac{\partial}{\partial x}(\bar{u}) = 0, \tag{14}$$

where the overbar means vertical integration over the whole domain. This implies that the mean flow is independent of x. Multiplying (14) by the depth of the layer H establishes that the mass flux is constant in space. We further require the mass flux to be independent of time to close the system, so that

$$(H\bar{u})_t = (H\bar{u})_{t=0}. \tag{15}$$

To use the condition (15) we will rewrite (8) with the use of (13):

$$\frac{\partial u}{\partial t} = -\frac{\partial uu}{\partial x} - \frac{\partial u\dot{\zeta}}{\partial \zeta} - \frac{\partial \phi_0}{\partial x} - \frac{\partial \phi_S}{\partial x} + fv. \tag{16}$$

The terms on the right-hand side of (16) can be calculated if $\mathbf{V}$ and θ are known, except for the unknown term $\partial\phi_0/\partial x$. Equation (16) is used to predict u without considering $\partial\phi_0/\partial x$ and condition (15) is applied to adjust Hu.

B. MODEL IMPLEMENTATION

The system of equations is solved with finite differences centered in space and time (leapfrog scheme). The nonlinear terms are formulated to conserve the total energy (potential plus kinetic). The Arakawa B (Arakawa and Lamb 1977) grid scheme is used in the x direction for hydrostatic consistency, so mass and momentum variables are

staggered. In the vertical, the energy conserving Lorenz (1960) scheme is applied where all variables but vertical velocity are placed in the middle of the layer, to represent the average of that layer. The vertical velocity grid points are set between the layers, and represent the interface changes. Figure 1 shows the arrangement of the variables in the grid system.

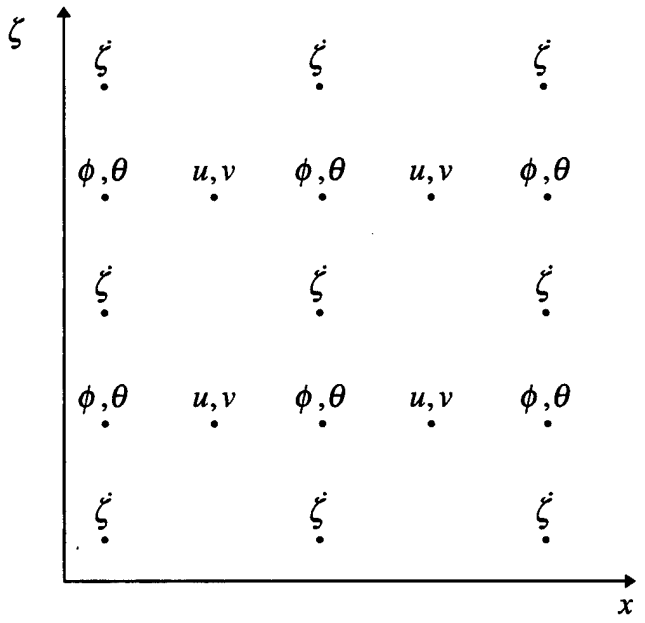

Figure 1. Model grid system following Arakawa and Lamb (1977) and Lorenz (1960).

The Matsuno scheme is applied periodically at time intervals to prevent solution separation. Convective dry adjustment is made when static instability is detected in the breakdown of waves. The constants and finite difference increments used in the model are displayed in Table 1. The grid spacing in the x direction is variable and is set to give the finest resolution in the position of the frontal formation. Figure 2 shows the horizontal grid spacing as a function of x. In the region of finest resolution, the horizontal increment

is 507 m. The time increment is variable between cases to satisfy the CFL condition because the waves propagate at different phase speeds depending on the static stability.

Table 1. Constants and finite difference increments employed in the model.

Parameter/Constant/Increment	Symbol	Value
Coriolis parameter	f	10^{-4} s^{-1}
Gravity acceleration	g	9.81 ms^{-2}
Reference potential temperature	θ_0	300 K
Reference pressure	p_0	1000 mb
Vertical domain	H	2000 m
Horizontal domain	W	3.7 10^6 m
Horizontal space increment (minimum)	Δx	507 m
Vertical space increment	$\Delta\zeta$	1/50
Time increment	Δt	variable
Initial static stability	$\partial\theta/\partial z$	variable
Initial temperature anomaly	$\Delta\theta$	variable

The numerical solutions are nondimensionalized in the following manner:

$$x' = x a_D\,, \qquad t' = f t\,, \qquad \theta' = \theta / \Delta\theta,$$

$$(u', v') = (u, v) / \left(\frac{g\Delta\theta H}{\theta_0}\right)^{\frac{1}{2}}\,, \qquad \dot{\zeta}' = \dot{\zeta} / \left[\frac{1}{a_D^{-1}}\left(\frac{g\Delta\theta H}{\theta_0}\right)^{\frac{1}{2}}\right],$$

where the primes denote the nondimensional variables and a_D^{-1} is the length scale of the initial temperature anomaly $\Delta\theta$. The vertical dimension ζ is already in nondimensional

form in the model. The variables hereafter referred are the nondimensional even though the primes are not shown.

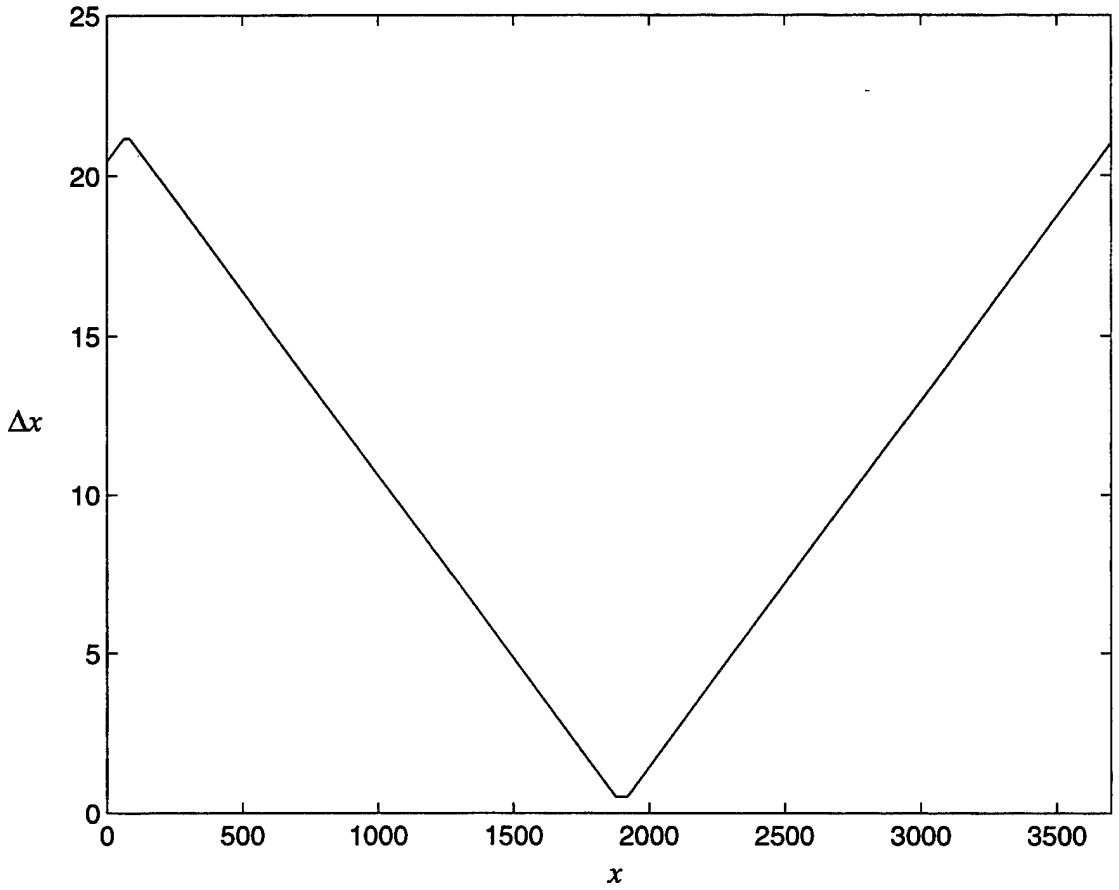

Figure 2. Horizontal grid spacing as a function of x. Both axis present the values in km. The finest resolution ($\Delta x = 507$ m) is located from $x = 1878$ km to $x = 1919$ km.

III. THEORY

A mass-momentum imbalance in a statically stable atmosphere will generate motion as the fluid tends toward a steady state thermal wind balance (Haltiner and Williams 1980; BW96). This geostrophic adjustment happens because the initial imbalance excites inertial gravity waves that carry energy away from the region of imbalance. The final state is dependent on whether the horizontal length scale (a_D^{-1}) of the region of imbalance is larger or smaller than the Rossby radius of deformation (L_R). The final state is determined by the initial mass field for the former case and by the initial wind field for the latter. The Rossby radius of deformation is defined as

$$L_R = \frac{c}{f},$$

where c is the speed of propagation of the appropriate gravity wave (see Haltiner and Williams 1980):

$$c = \frac{H N}{\pi}, \tag{17}$$

and N is the Brunt-Väisälä frequency, defined by:

$$N = \sqrt{\frac{g}{\theta_0}\frac{\partial \theta}{\partial z}},$$

which yields

$$L_R = \frac{HN}{\pi f}. \tag{18}$$

Unless friction is considered, the gravity waves produce a periodic oscillation about the geostrophic balance of constant amplitude in a limited domain. In an infinite domain, the gravity waves propagate away from the imbalance region, leaving a state of geostrophic balance. In a simple unbalanced initial state, there is a temperature gradient and the velocity field is zero. As a result of the imbalance between the mass and momentum fields, a transient velocity field develops and helps to further intensify the temperature gradient. When the motion is independent of y, u is the divergent part of the wind field and v is the rotational part of the wind. The divergent wind causes horizontal convergence in the region of maximum temperature gradient which intensifies the gradient and enhances upward motion. This nonlinear effect does not happen in quasi-geostrophic and linear models. Williams (1972) suggests that the nonlinear results are due to ageostrophic effects and these effects tend to accelerate frontal formation. The linear models indicate the formation of a temperature discontinuity only as $t \rightarrow \infty$ while nonlinearity can produce a front within a finite period of time. Another nonlinear effect is the tilting of the front toward the cold air, which is important to avoid a superadiabatic lapse rate in the warm sector.

The result of the geostrophic adjustment is different near the upper and lower boundaries than away from it. Without the influence of the boundary and for positive values of static stability, the geostrophic adjustment is a function of the initial wind field ($a_D^{-1} < L_R$) or a function of the initial mass field ($a_D^{-1} > L_R$). In the former case, the gravity

waves remove energy from the imbalance region and the temperature gradient decreases because the initial wind is zero in the simple case previously mentioned. The larger the static stability, the faster the gradient decreases, since the vertical motion plays an important role in the temperature change. Near the upper and lower boundaries, the vertical motion is much smaller and the temperature changes are much less during geostrophic adjustment. When the nonlinear terms are used, the gradient increases near the boundaries and the front tilts toward the cold air, in a more realistic fashion.

Depending on the characteristics of the fluid, the existence of a material boundary can cause the temperature gradient to collapse into a front near that boundary, instead of oscillate. The formation of a temperature discontinuity in a steady state atmosphere depends on the characteristics of the fluid as defined by the Rossby (*Ro*) and the Froude (*F*) numbers (Williams 1967; BW96) . For $f \neq 0$, they can be defined as

$$Ro = \frac{\sqrt{gH\Delta\theta/\theta_0}}{f a_D^{-1}}, \tag{19}$$

$$F = \frac{\sqrt{gH\Delta\theta/\theta_0}}{NH}. \tag{20}$$

Another way of characterizing the flow is by using the Rossby and the Burger number (*B*), which is the ratio *Ro/F* and can be written

$$B = \frac{HN}{f a_D^{-1}}. \tag{21}$$

Equations (18) and (21) can be combined to allow:

$$\frac{L_R}{a_D^{-1}} = \frac{B}{\pi}, \tag{22}$$

and thus B/π is a measure of the adjustment regime for the fluid.

The definition of a frontal formation in a numerical experiment in not a mere objective task. This is particularly true for marginal cases since there is no clear cut between the frontal and nonfrontal regimes. A useful way to quantify the intensity of the front is the d-value (d), used by Williams (1967;1972;1974) and Williams et al. (1992). It can be defined as

$$d = \frac{\Delta\theta}{a_D^{-1}\left|\partial\theta/\partial x\right|_{max}}. \tag{23}$$

If all the temperature change happened in one grid spacing, as seen in Figure 3, $d \rightarrow \Delta x / a_D^{-1}$, as a result of the discretization of the domain. Since d is a measure of the temperature gradient and no friction is considered, it is expected to oscillate when no frontogenesis occurs and to collapse ($d \rightarrow \Delta x / a_D^{-1}$) when a front forms. Since Δx imposes a constraint for d in the frontal cases, different grid sizes can be used for the same type of flow to assess whether or not a front has occurred. It is also important to verify the number of grid spaces involved in a frontal region since the collapse is expected to behave as in Figure 3.

BW96 derived a time-dependent analytic solution for the mass and momentum fields that applies to level boundaries where $w = 0$. They used momentum coordinates

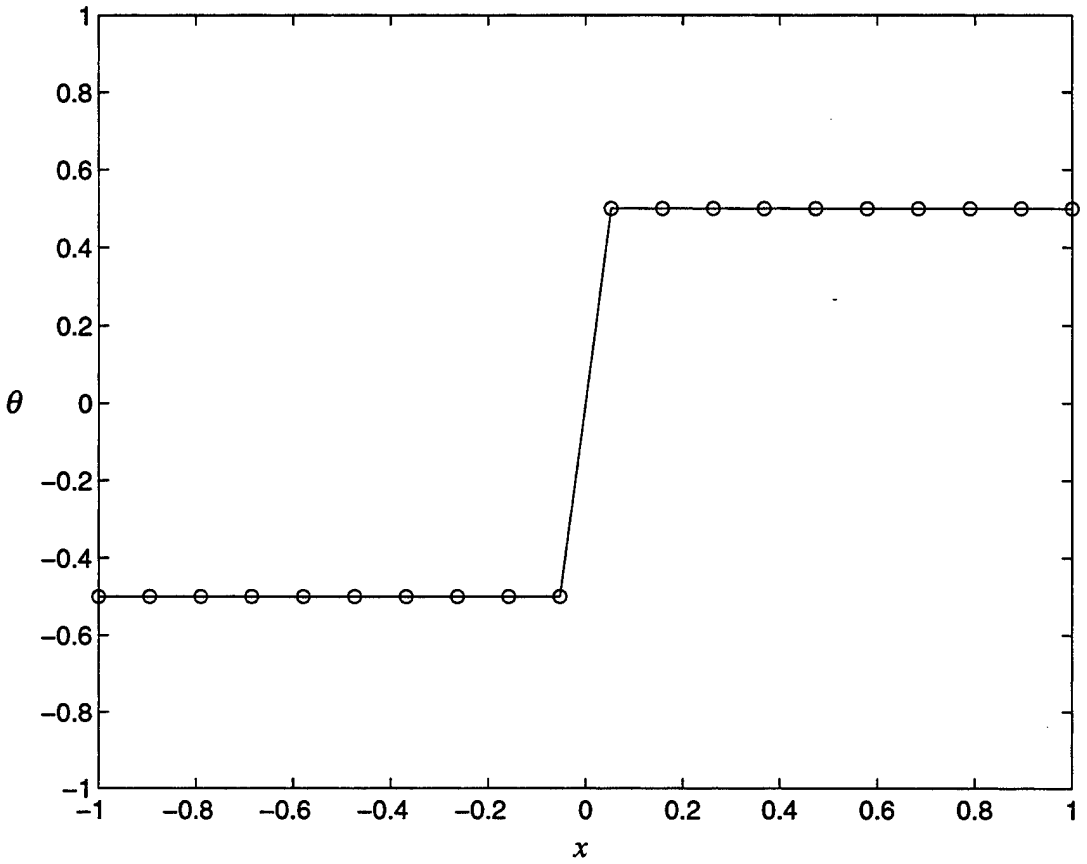

Figure 3. Hypothetical temperature distribution in a frontal zone. The circles represent grid points.

following Hoskins and Bretherton (1972):

$$X = x + v, \tag{24a}$$

$$Z = z, \tag{24b}$$

$$T = t, \tag{24c}$$

where X is conserved ($dX/dt = 0$), as obtained by substituting (24a) in their y-momentum

equation. The use of a domain independent of y allows them to write the momentum equations, in nondimensional form, as

$$\frac{\partial u}{\partial t}+u\frac{\partial u}{\partial x}+w\frac{\partial u}{\partial z}-v'=0, \tag{25}$$

$$\frac{\partial v'}{\partial t}+u\frac{\partial v}{\partial x}+w\frac{\partial v}{\partial z}+u=0, \tag{26}$$

where $v = v_g + v'$, and v' is the ageostrophic velocity. The horizontal pressure gradient force is balanced by the geostrophic wind.

The transformation of (25) into momentum coordinates yields

$$\frac{\partial u}{\partial T}+u\frac{\partial u}{\partial X}+w\frac{\partial u}{\partial Z}-v'+\frac{\partial u}{\partial X}\left(\frac{\partial v'}{\partial t}+u\frac{\partial v}{\partial x}+w\frac{\partial v}{\partial z}\right)=0. \tag{27}$$

Substituting (26) into (27) leads to

$$\frac{\partial u}{\partial T}+w\frac{\partial u}{\partial Z}-v'=0. \tag{28}$$

Following the same process, (26) can be expressed as

$$\frac{\partial v'}{\partial T}+w\frac{\partial v}{\partial Z}+u=0. \tag{29}$$

The solution of v' for the system (28)-(29), when $w = 0$ (at $\zeta = 0, 1$) , has the form

$$v' = A(X)\sin T + B(X)\cos T.$$

The initial conditions are $u = v = 0$, such that on the vertical boundaries

$$v'(X) = -v_g(X),$$

$$\frac{\partial v'(X)}{\partial T} = 0.$$

Therefore, the solution becomes

$$v' = -v_g \cos T,$$

and the total rotational wind solution is

$$v = v_g(1 - \cos T). \tag{30}$$

Blumen and Wu (1994) give the condition for frontogenesis following Hoskins and Bretherton (1972) as

$$1 - \frac{\partial v}{\partial X} = 0, \tag{31}$$

and substituting (30) into (31) leads to the general condition for frontal formation

$$(1 - \cos T)\frac{\partial v_g}{\partial X} = 1. \tag{32}$$

For the zero potential vorticity case, the solution for the geostrophic flow can be expressed as

$$v_g = -\frac{\partial \theta_0}{\partial x_0}\left(\frac{1}{2} - Z\right) \tag{33}$$

Substitution of (33) into (32) gives the particular condition for frontal formation on the boundaries when the potential vorticity is zero

$$(1-\cos T)\frac{\partial^2\theta_0}{\partial x_0^2}=-2, \tag{34}$$

since $\partial/\partial X = \partial/\partial x_0$. Using an initial temperature distribution of the form

$$\theta_0(x_0)=\frac{1}{2}erf(Ro\,x_0), \tag{35}$$

equation (34) can be rewritten by going back to dimensional quantities

$$1-\cos(ft)=\frac{(2\pi e)^{1/2}}{Ro^2}. \tag{36}$$

Blumen and Wu (1994) used the steady state version of this equation which has no cosine to compute the critical value of Ro = 2.03. BW96 included the time dependent part of (36) which shows that the minimum Ro is given by

$$(Ro)_c=\frac{2.03}{\sqrt{2}}=1.435,$$

and it occurs at $t_c = \pi f^{-1}$. This is the limiting case for large Froude number.

The authors also derived a more general time-dependent solution for d. The dimensional temperature gradient necessary for solving (23) is given, in momentum coordinates, by

$$\left(\frac{\partial\theta}{\partial x}\right)_D = \frac{\Delta\theta}{a_D^{-1} Ro}\frac{\partial\theta_0}{\partial x_0}\frac{1}{1-\partial v/\partial x_0}.$$

Using (30), (33), and (35) leads to

$$\left(\frac{\partial\theta}{\partial x}\right)_D = \frac{\Delta\theta\, a_D\, \pi^{-1/2}\, e^{-(Rox_0)^2}}{1-\frac{4}{\pi^{1/2}}\left(\frac{g\Delta\theta H}{\theta_0 a_D^{-2}}\right)\left(\frac{1}{2}-Z\right)\frac{\sin^2(ft/2)}{f^2} Rox_0\, e^{-(Rox_0)^2}}. \tag{37}$$

The maximum temperature gradient can be found by differentiating (37) with respect to $Ro\,x_0$ and setting the result to zero, which gives

$$(Rox_0)_{max} = 2\frac{g\Delta\theta H}{\theta_0 a_D^{-2}\pi^{1/2}}\left(\frac{1}{2}-Z\right)\frac{\sin^2(ft/2)}{f^2} e^{-(Rox_0)^2_{max}}. \tag{38}$$

Equation (38) can be solved iteratively for Rox_0, which finds the value at the point of maximum temperature gradient for a given time. The d-value is found by substituting (38) into (37), and using (23)

$$d = \frac{1-2(Rox_0)^2_{max}}{\pi^{1/2} e^{-(Rox_0)^2_{max}}}. \tag{39}$$

Equations (38) and (39) also allow the calculation of the time for a front to form. Analytical frontogenesis occurs when $d \to 0$ which leads to $(Rox_0)^2_{max} = 1/2$. The time for frontal formation can thus be calculated with the use of (38).

The time evolution of their solution is shown in Figure 4 for the limiting case. It does not consider the barotropic pressure contribution, which is not very significant for large temperature forcing associated with frontogenesis. However, this term is important for weak forcing. The initial d-value is $d = \sqrt{\pi}$.

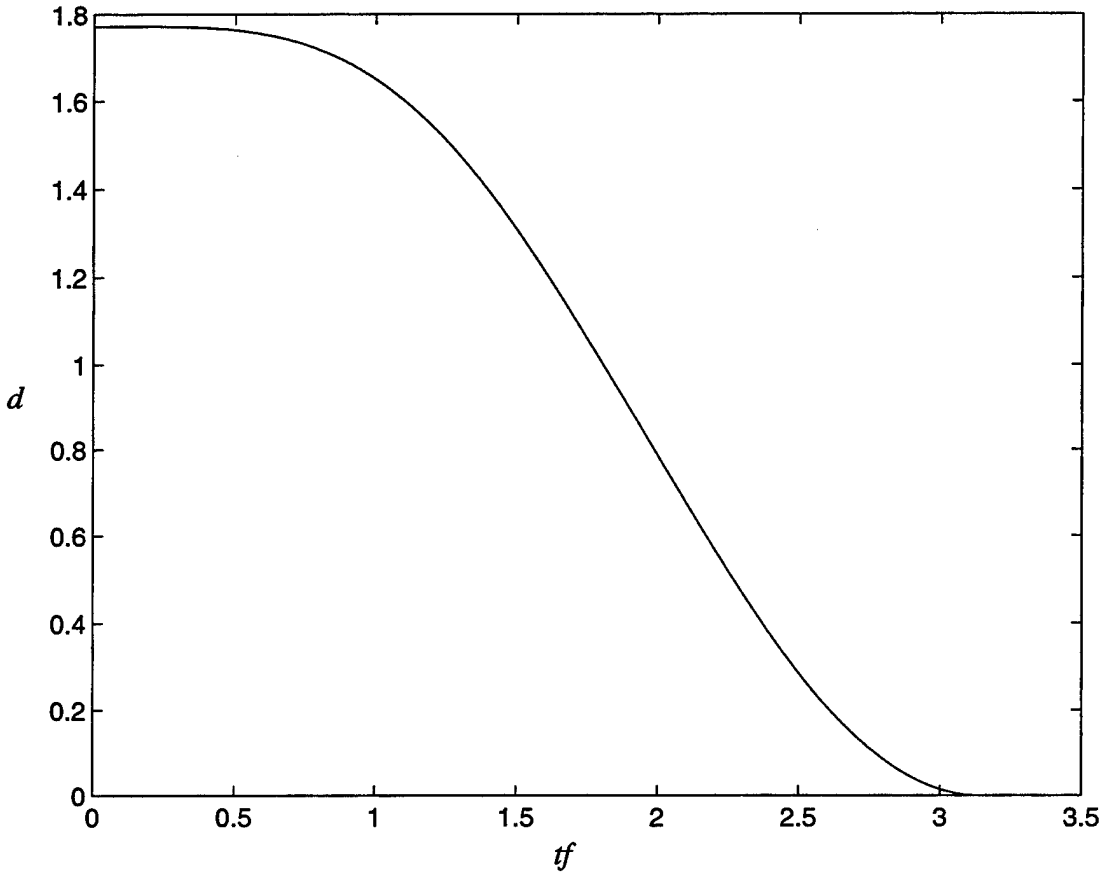

Figure 4. Time evolution of the d-value for the analytical solution of BW96. It applies to the limiting case of frontal formation, for zero potential vorticity. The critical time in this limit is $t = \pi f^{-1}$ when the analytical solution collapses.

Figure 5 shows some marginal cases of frontal formation as suggested by Blumen (personal notes, here denoted Blumen) in a $Ro \times F$ plot (Figure 5a is a log-log plot and Figure 5b is a linear plot corresponding to the inset in 5a). Blumen extended the analytic

theory in BW96 to the stratified solution in Blumen and Wu (1994). The solutions in Blumen and Wu (1994) are steady state solutions in geostrophic momentum coordinates. The initial state in physical space is the linear geostrophic adjustment solution which would result from the initial state used in this thesis. The correction for the time dependent factor gives $Ro/\sqrt{2}, F/\sqrt{2}$. These cases are displayed as circles and the solid line is an exponential fit for those points. Frontogenesis occurs for atmospheric flows whose *Ro* and *F* are located on the concave region of the graph (Region II). The points on

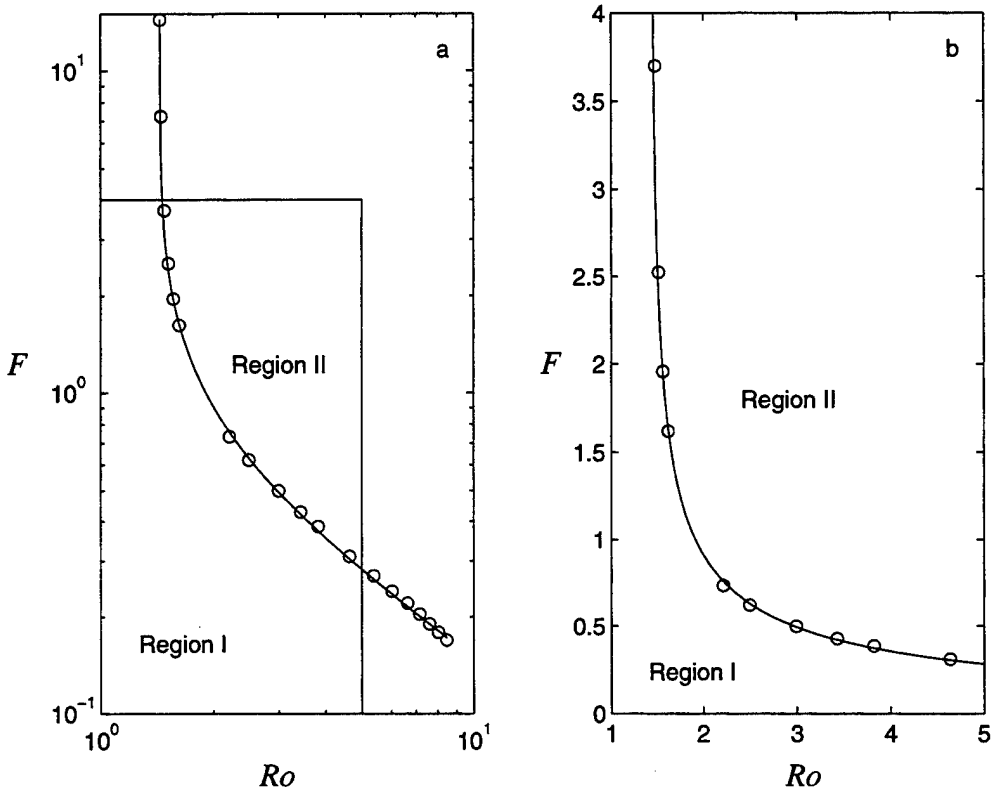

Figure 5. Blumen's cases for marginal frontogenesis marked as circles. The solid line is an exponential fit for those points. Region I represents the nonfrontal cases and Region II the frontal ones. (a) is a log-log plot and (b) is a linear plot corresponding to the inset in (a).

the other side of the curve (Region I) represent flows where geostrophic adjustment and inertial oscillation occur without collapsing into a front.

IV. INITIAL AND BOUNDARY CONDITIONS

The initial temperature field has an anomaly component which is a function of the initial position of the maximum temperature gradient (x_0) superimposed on a reference temperature that varies with height at a constant positive rate $\partial\theta/\partial z$:

$$\theta = \frac{N^2}{g} z + \theta_0(x).$$

The anomaly component has an error function distribution defined as

$$\theta_0 = \frac{\Delta\theta}{2} erf\left[(x - x_0)a_D\right], \tag{40}$$

where *erf* is the error function. The initial position x_0 is selected for each case in such a way as to obtain the minimum d-value in the region of minimum horizontal grid spacing. Lower temperatures lie on the western portion of the domain. Since the amplitude of the error function is 2, the amplitude of (40) is given by $\Delta\theta$. The temperature distribution given by (40) is seen in Figure 6, as a function of $x - x_0$. The initial momentum field is zero and thus is out of geostrophic balance with the mass field.

The assumption that the atmosphere is incompressible and the use of an antisymmetric temperature field will lead to antisymmetric solutions on the upper and lower boundaries. There is in fact a small difference between the solutions on both boundaries due to the different grid spacing such that the fronts will form in regions of different resolution. Since the lower front will form in a region of finer resolution, the

numerical solution there will be more accurate. Therefore, the lower boundary processes will be described in this work, even though it applies to the upper boundary as well.

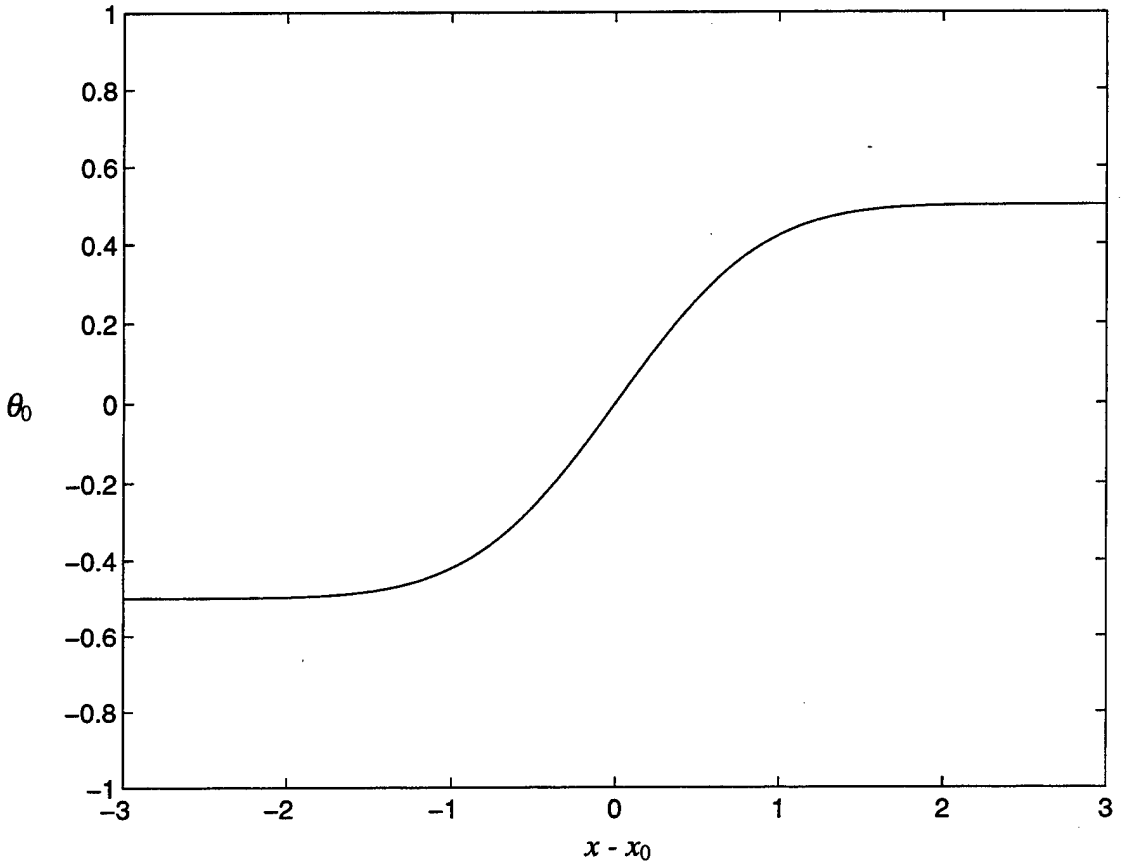

Figure 6. Initial temperature anomaly as defined by equation (40), as a function of $x - x_0$.

The model uses variable grid size in the horizontal to give a fine resolution in the region of interest. The horizontal domain is large enough to preserve the region of imbalance from lateral boundary effects. The boundaries are far enough so gravity waves cannot reach them. Zero vertical velocity condition is used on the vertical boundaries. The model uses periodic lateral boundary conditions and two symmetric temperature gradient regions to match the temperature in those boundaries. One of the regions is in

thermal wind balance with the initial wind field and does not change during the integration period. Only the unbalanced region is depicted in this study.

V. NUMERICAL SOLUTIONS

The starting point for this investigation is the Blumen's curve shown in Figure 5. The work consists of integrating the model for several cases, whose characteristics are described by *Ro* and *F*. For convenience, all the parameters of the fluid (listed in Table 1) are held constant, except the initial temperature anomaly ($\Delta\theta$) and the static stability ($\partial\theta/\partial z$). The nondimensional numbers *Ro* and *F* of every case allow the calculation of $\Delta\theta$ and $\partial\theta/\partial z$, by using equations (19) and (20). For each situation, two different horizontal grid spacings are used to help determine whether or not a front occurs. The minimum grid spacing in one is twice as large as the minimum for the other. Therefore, the *d*-value in the former is expected to be roughly twice the value of the latter for a front. If there is no front, the values will be the same.

Figure 7 shows the selected cases (circles) for this study and the curve fit (solid line) for Blumen's points, as displayed in Figure 5. The dashed line represents $B = \pi$ that separates the two different regimes of geostrophic adjustment in large ($a_D^{-1} > L_R$) and small ($a_D^{-1} < L_R$) scale processes, obtained from setting $L_R/a_D^{-1} = 1$ in equation (22). The two lines divide the domain in four regions. In regions I and II there is no frontal formation, while near-boundary fronts occur in regions III and IV. Regions I and III are characterized by large scale geostrophic adjustment whereas the small scale adjustment occurs in regions II and IV.

Section A presents the analysis of the zero potential vorticity (large *F*) atmosphere to compare with the numerical and analytical solutions of BW96. Examples of the four

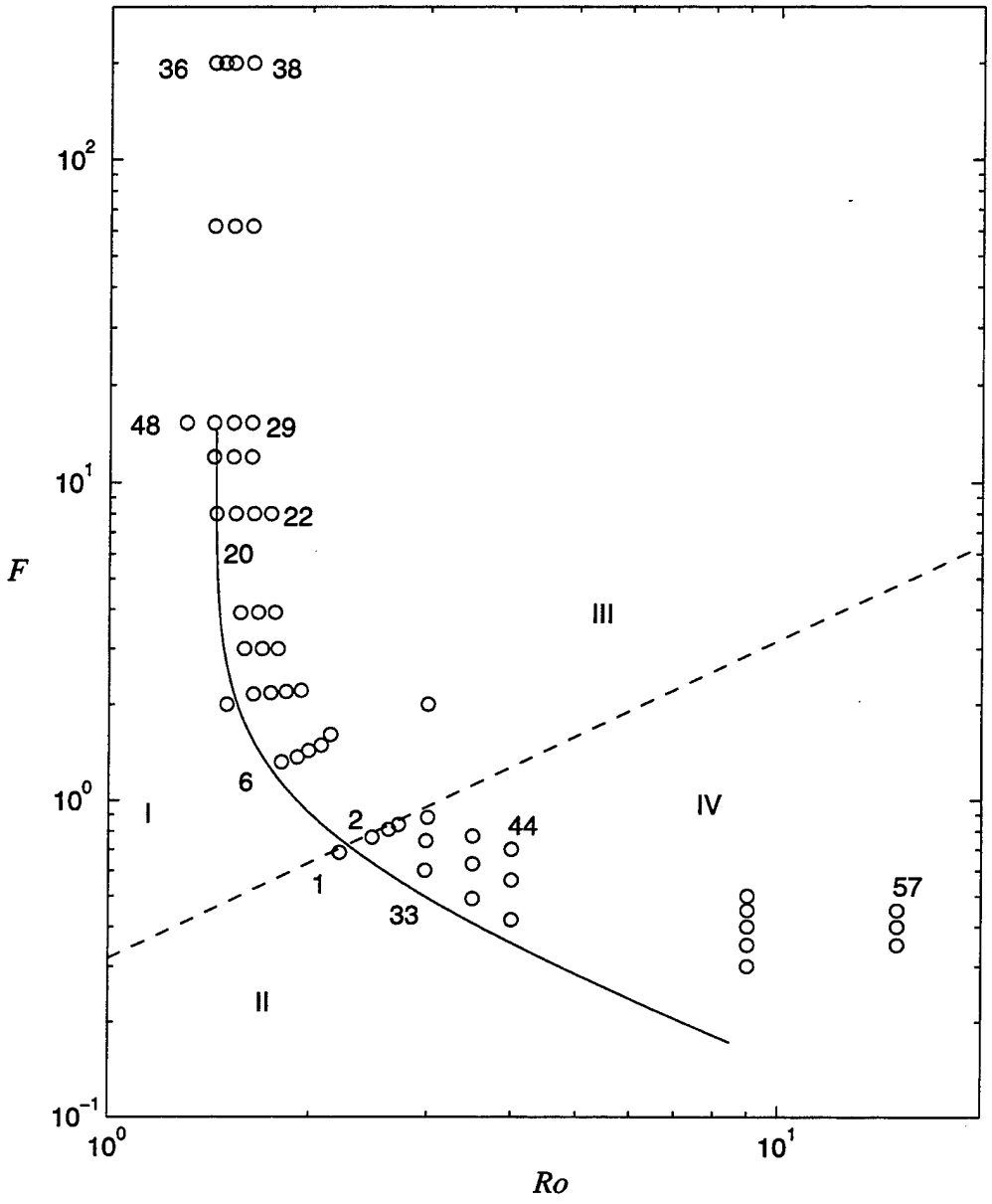

Figure 7. Distribution of cases in the present study (circles) and the exponential fit for Blumen's cases (solid line). The dashed line represents $B = \pi$ (separation of large- and small-scale geostrophic adjustment). The axes are in logarithm scale. The two lines separate the domain in four regions, shown in roman. The numbers identify the closest circle and will be refered in the next sections.

regions shown in Figure 7 are presented in the next four sections. The transition zone between large- and small-scale geostrophic adjustment and between frontal and

nonfrontal regions are discussed in section F. The zero planetary vorticity case is analyzed in section G to compare to a large-*Ro* nonzero case.

A. ZERO POTENTIAL VORTICITY

The main characteristic of the zero potential vorticity ($F \rightarrow \infty$) atmosphere is that gravity waves cannot propagate away from the imbalance region due to the absence of vertical stability. This means that the mid-level region (away from the upper and lower boundaries) does not show a significant change except for the tilting of the isothermals. The model levels near the vertical boundaries, however, do suffer significant modification. The larger the *Ro*, the more these levels change.

Figure 8 shows the time evolution of the *d*-value for case 36 (Ro = 1.43). The solid line is the numerical value, and the dashed line is the analytic solution obtained from equations (38) and (39). There is no front and the temperature gradient oscillates with period $2\pi f^{-1}$ (the inertial period). Although the period of oscillation matches, the amplitude differs due to the absence of the barotropic term in the analytic solution of the *d*-value. The temperature anomaly and the rotational wind component are displayed in Figure 9, for $t = \pi f^{-1}$. The divergent component of the wind is zero at that time.

If the temperature forcing is sufficient to form a front, as in case 38 (Ro = 1.63), the inertial oscillation is interrupted because of the temperature jump. Figure 10 depicts the time evolution of the *d*-value for this case. The solid line is the numerical value, and the dashed line is the analytic solution obtained from equations (38) and (39). Again, the absence of the barotropic term in the analytic solution of the *d*-value causes a difference between the numerical and the analytic solutions. For frontal cases, the analytic solution

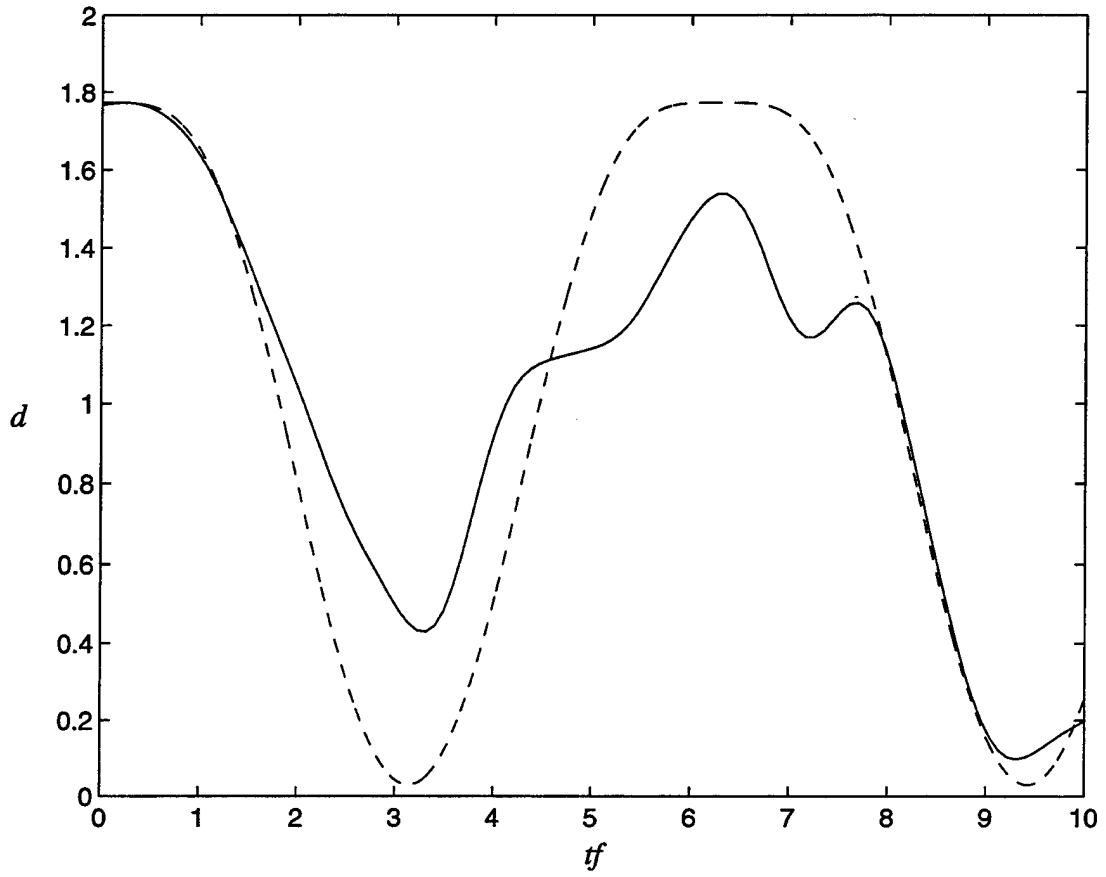

Figure 8. Time evolution of d for the zero potential vorticity case (no front). The solid line is the numerical value, and the dashed line is the analytic solution. The period of oscillation is $2\pi f^{-1}$ (the inertial period).

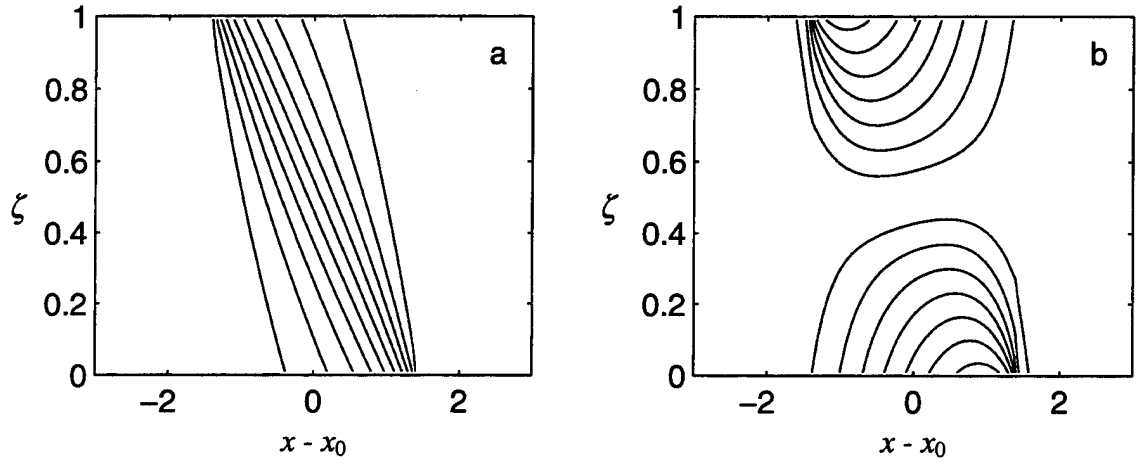

Figure 9. The (a) temperature anomaly and (b) rotational component (v) of the wind for $t = \pi f^{-1}$ (no front). The divergent component of the wind is zero at that time. The contour interval in (b) is 0.1 and the zero line is removed for clarity. The maximum southerly wind occurs in the lower boundary.

precedes the numerical as shown by BW96. The temperature anomaly and the rotational wind component, for case 38, are displayed in Figure 11, for $t = 2.7f^{-1}$. The divergent component of the wind tends to zero at that time.

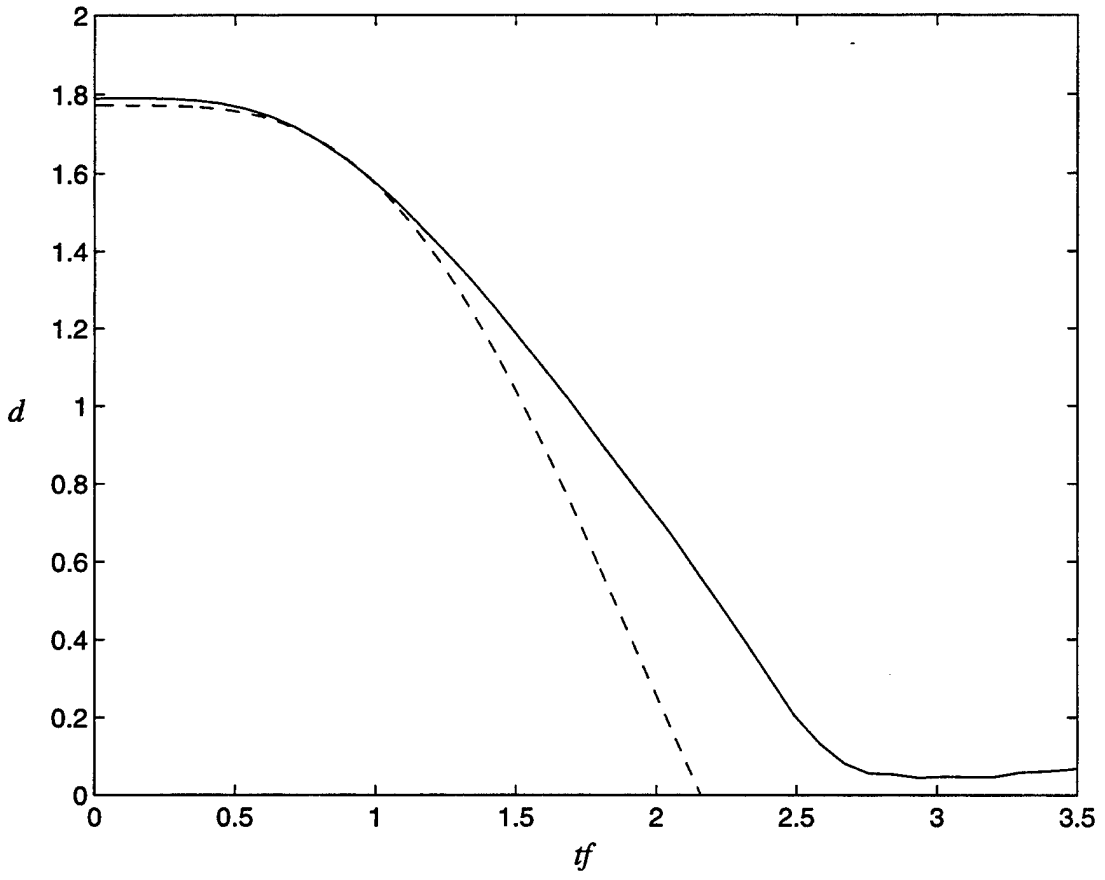

Figure 10. Time evolution of *d* for the zero potential vorticity case, with frontal formation. The solid line is the numerical value, and the dashed line is the analytic solution for the zero potential vorticity frontal formation.

B. NO FRONT - LARGE-SCALE ADJUSTMENT (REGION I)

The time evolution of the total temperature gradient of point 48 is presented in Figure 12. The fluid initially has $Ro = 1.3$ and $F = 15.3$. The temperature gradient increases at the boundaries as the zone of maximum gradient moves toward the warmer

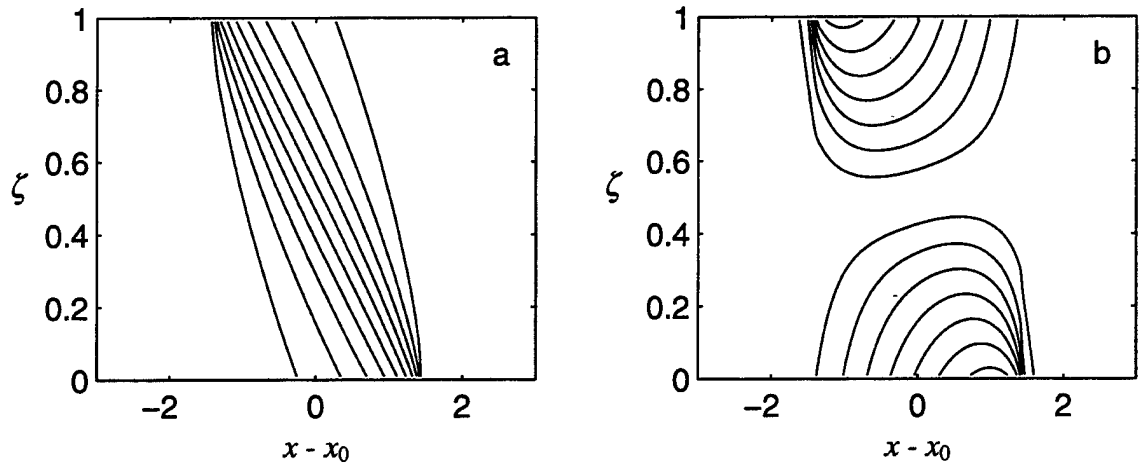

Figure 11. The (a) temperature anomaly and (b) rotational component (v) of the wind for $t = 2.7f^{-1}$, with frontal formation. The divergent component of the wind tends to zero at that time. The contour interval in (b) is 0.1 and the zero line is removed for clarity. The maximum southerly wind occurs in the lower boundary.

air in the lower boundary and toward the colder air in the upper one (the axis of maximum gradient tilts so that the colder air is underneath). The oscillatory nature of the temperature distribution can be noticed by comparing the cross-sections at $t = 0$ and $t = 2\pi f^{-1}$. This case is very similar to that shown in section A, despite the large difference in F.

Figure 13 displays the d-value evolution with time for the levels (a) $\zeta = 0$ and (b) $\zeta = 0.5$. The changes in the maximum temperature gradient at the former level are much larger than those in the latter. The static stability is very small and gravity waves are very slow, which results in very little energy propagating away from the initial imbalance region. The main cause of temperature distribution change is due to the divergent part of the wind (u), near the vertical boundaries. Figures 14 and 15 show the wind distribution (u and v respectively) associated with the temperature distribution in Figure 12. The

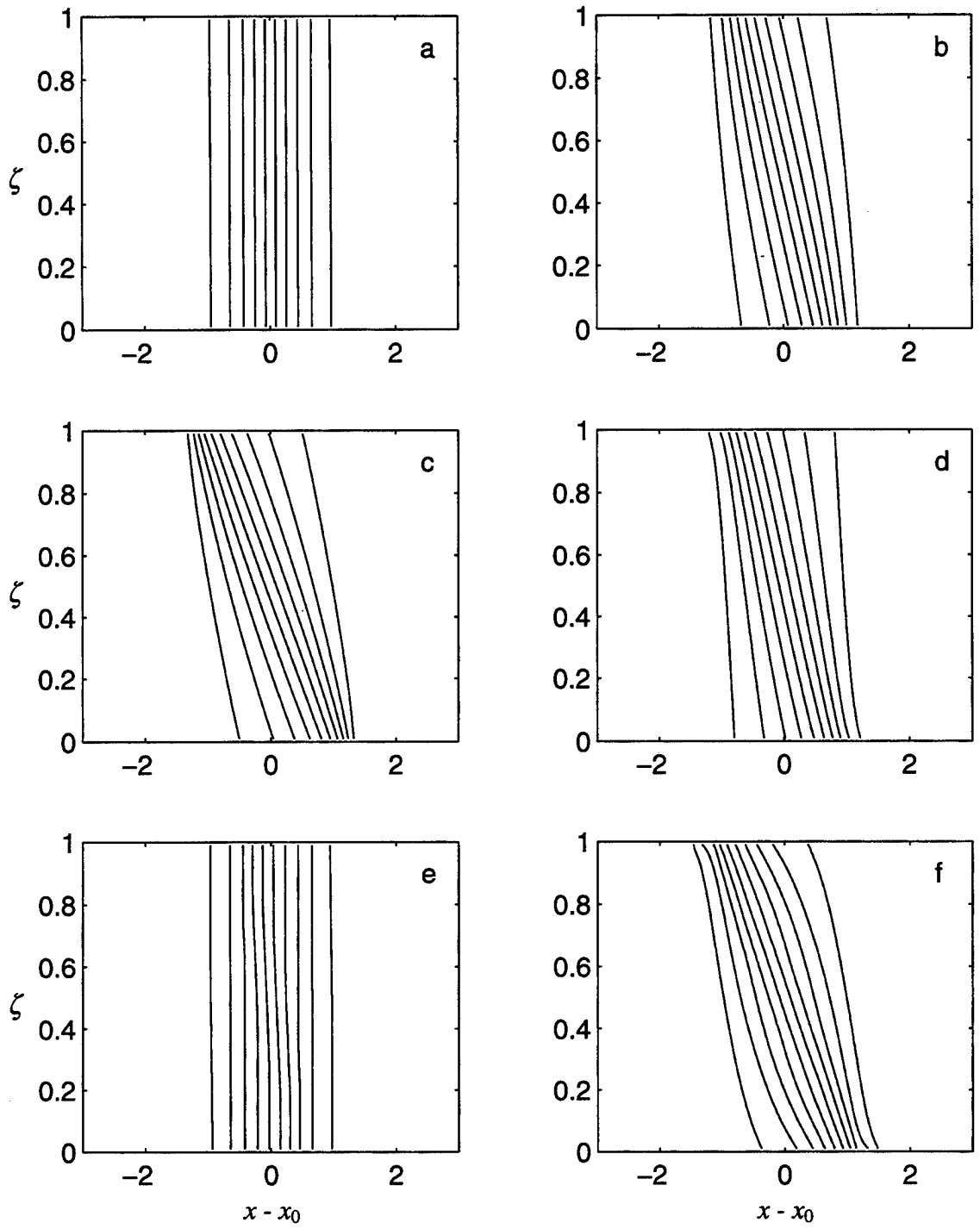

Figure 12. Time evolution of the total temperature cross-section for point 48 in Figure 7, for (a) $t = 0$, (b) $t = 1.8f^{-1}$, (c) $t = \pi f^{-1}$, (d) $t = 4.7f^{-1}$, (e) $t = 2\pi f^{-1}$, and (f) $t = 9.8f^{-1}$.

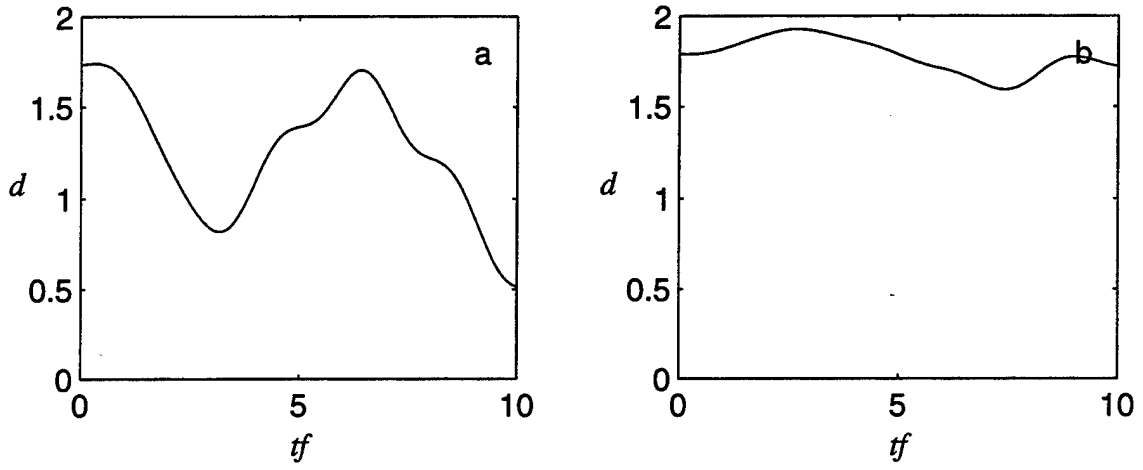

Figure 13. Time distribution of d-value (case 48) for levels (a) $\zeta = 0$ and (b) $\zeta = 0.5$.

u-component works both to intensify the temperature gradient when it is small and to diminish it when it is strong, causing the oscillation seen in Figure 13. This component shifts sign in the points of maximum and minimum d-value. The rotational component anomaly (v), on the other hand, attains its maximum (minimum) when and where the temperature gradient is maximum (minimum). Both components are nearly zero in the vicinity of the level $\zeta = 0.5$. This relationship is depicted in Figure 16 that shows the time series for the point where the d-value is calculated (maximum temperature gradient), in the lower boundary. As a result of the inhomogeneous surface convergence, the temperature distribution near the boundaries loses the antisymmetric characteristic as seen in Figure 17, at $t = 0$ and $t = \pi f^{-1}$.

The use of a grid spacing with the minimum Δx twice as large as the previous one results in similar fields and d-value. The other points in this region also show analogous behavior except that the points with larger Ro have a small decrease in the temperature gradient near $\zeta = 0.5$. In these cases, the oscillation can be noticed in the tilt of the

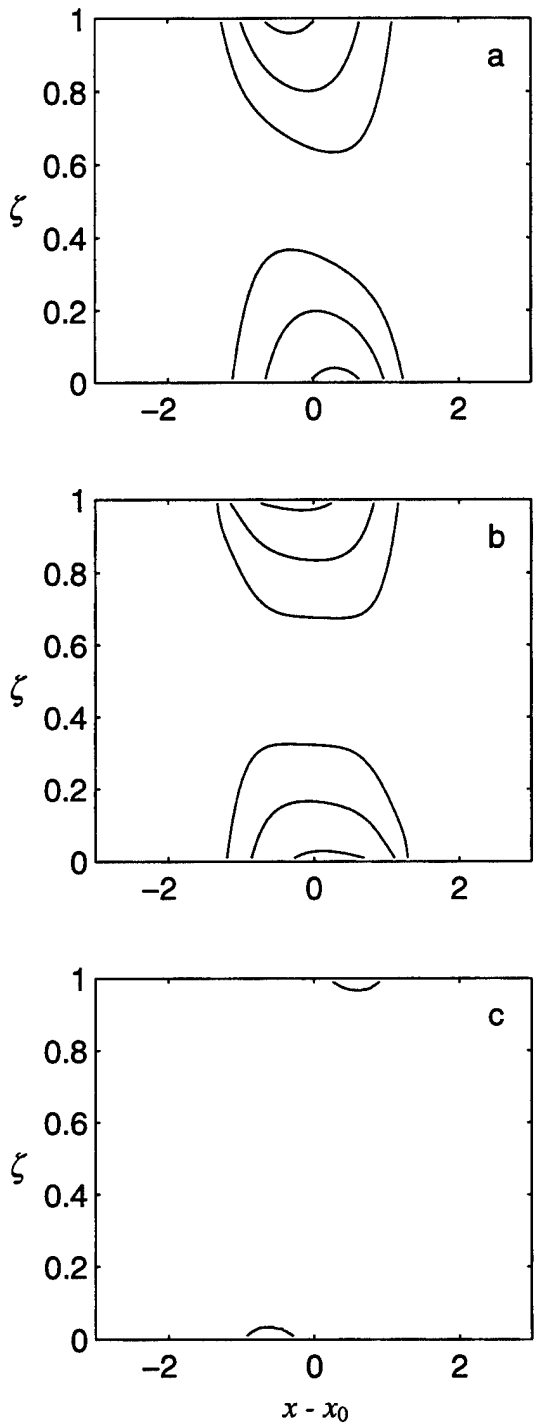

Figure 14. Time evolution of u for point 48, for (a) $t = 1.8f^{-1}$, (b) $t = 4.7f^{-1}$, and (c) $t = 9.8f^{-1}$. The u field is nearly zero for the other times in Figure 11. The isoline interval is 0.1. In the lower boundary, u is positive in (a), and negative in (b) and (c). The zero isoline is removed for clarity.

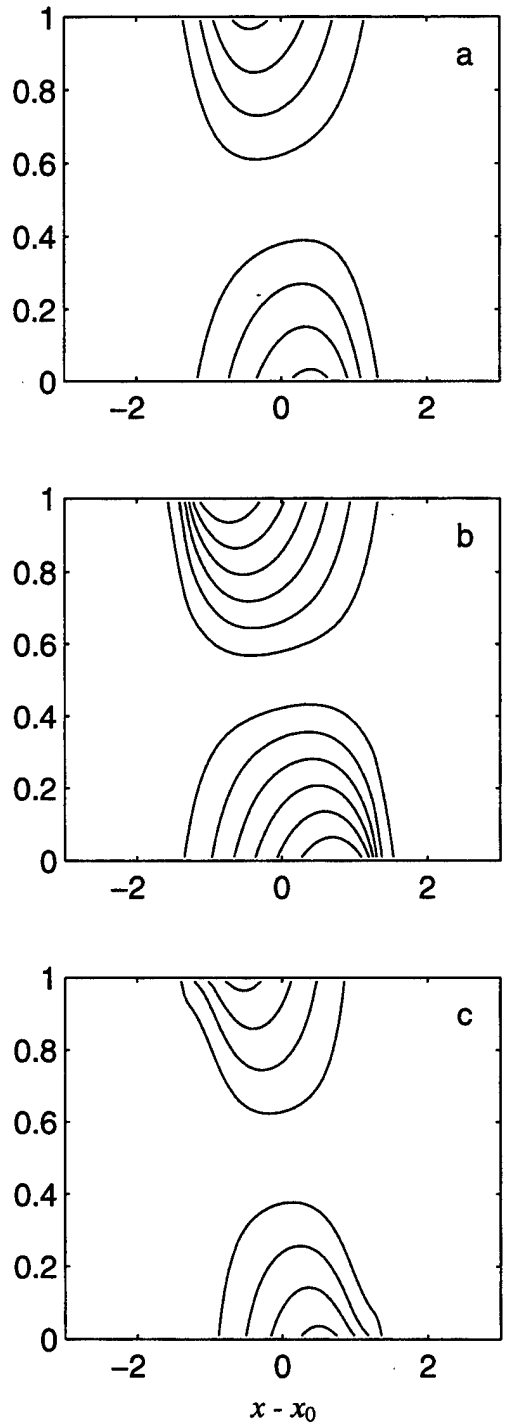

Figure 15. Time evolution of v for point 48, for (a) $t = 1.8f^{-1}$, (b) $t = \pi f^{-1}$, and (c) $t = 4.7f^{-1}$. The v field is zero for $t = 0$ and $t = 2\pi f^{-1}$, and very similar to (b) for $t = 9.8f^{-1}$. In the lower boundary, v is negative in the three frames. The zero isoline is removed for clarity.

isotherms. Another difference is the change in the period of oscillation that decreases as *Ro* increases, but no difference is observed when *F* changes.

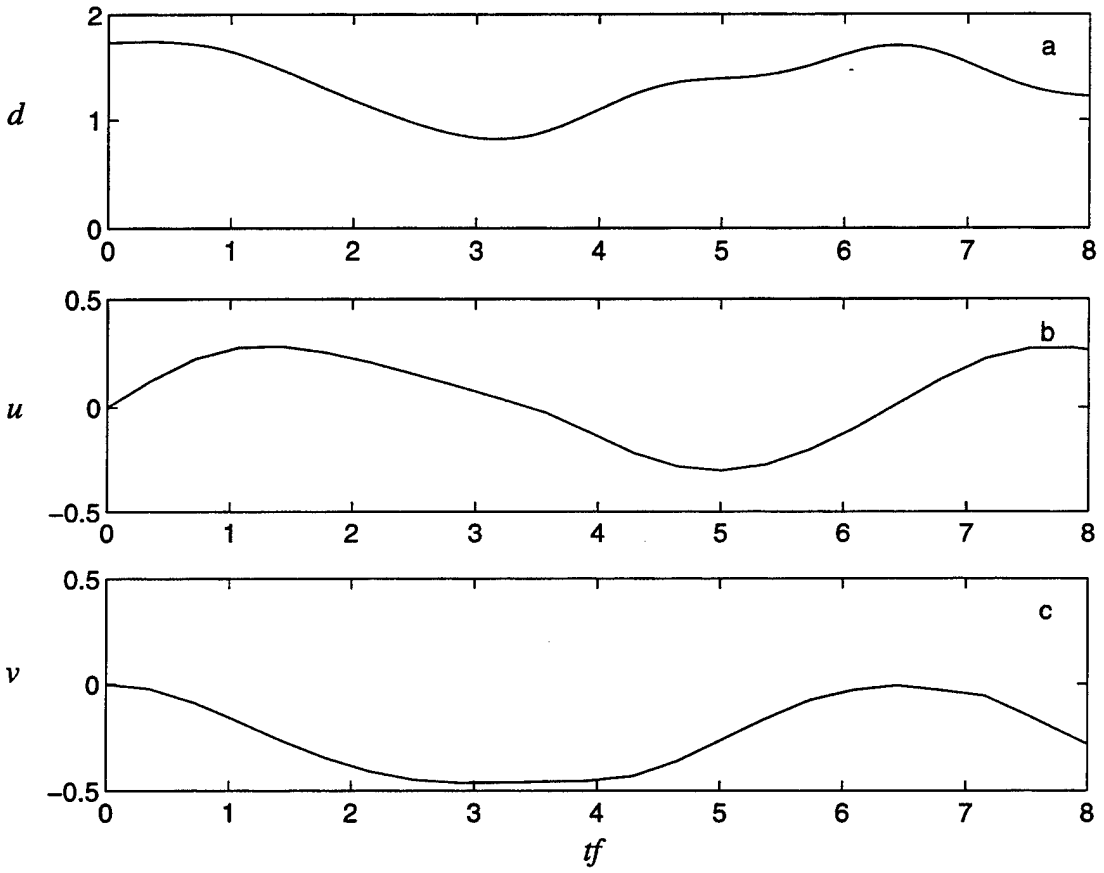

Figure 16. Time series for (a) *d*-value, (b) *u*, and (c) *v* in the point of maximum temperature gradient, in the lower boundary (case 48).

C. NO FRONT - SMALL-SCALE ADJUSTMENT (REGION II)

Figures 18 and 19 show the time variation of the temperature field of point 33 (see Figure 7), which has $Ro = 2.975$ and $F = 0.602$. The former presents the total temperature whereas the latter depicts the temperature anomaly field. The main feature of this case is the tendency of the temperature gradient, away from the boundaries, to be strongly

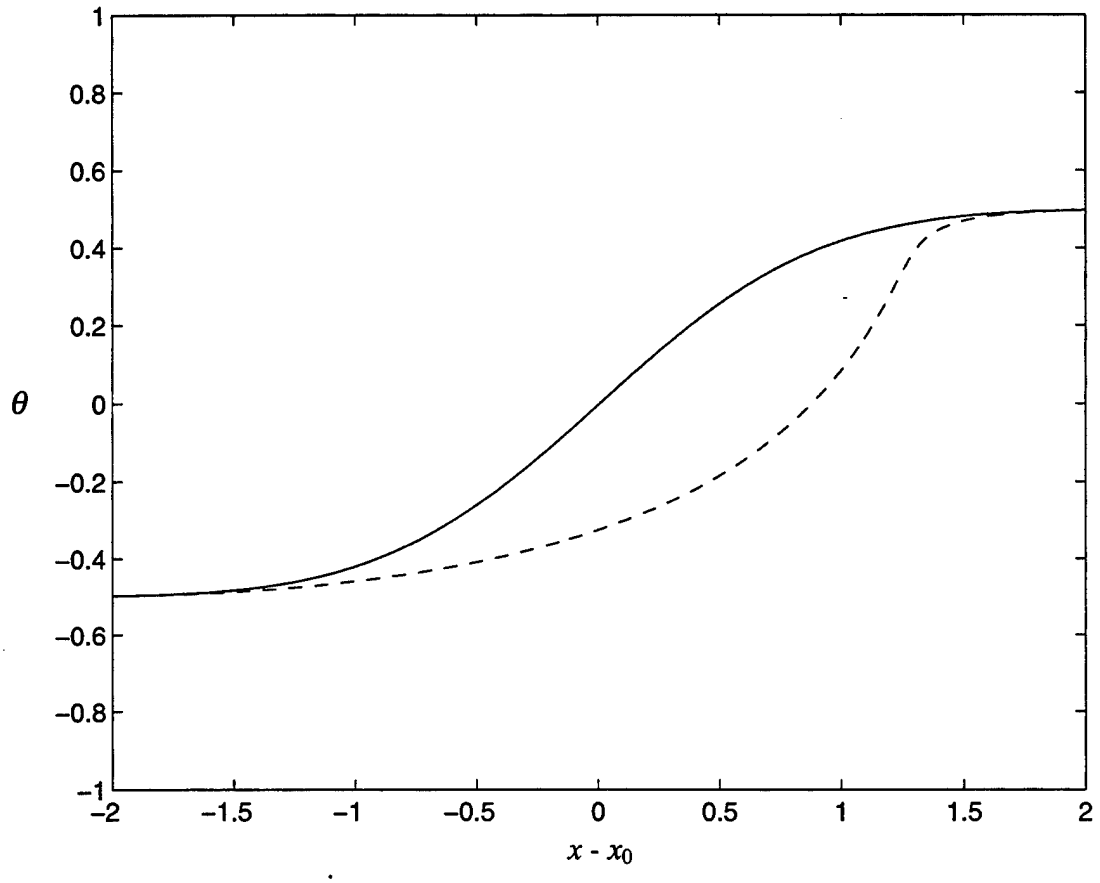

Figure 17. Temperature profile for the lowest level, at $t = 0$ (solid line) and $t = \pi f^{-1}$ (dashed line).

damped. This is expected since in this region the steady state solution is a function of the initial momentum field, which is initially zero. Therefore, in the long run, the temperature gradient will tend to vanish.

The temperature gradient in the lower boundary, on the other hand, behaves the same way as in region I, where the key player is the divergent wind field. Figure 20 shows the *d*-value for the lower boundary, where the characteristic oscillation is seen. The period is much smaller than that of region I. The *d*-value for the mid-level region is not a good indication in this case because the gravity waves become very fast and distort the

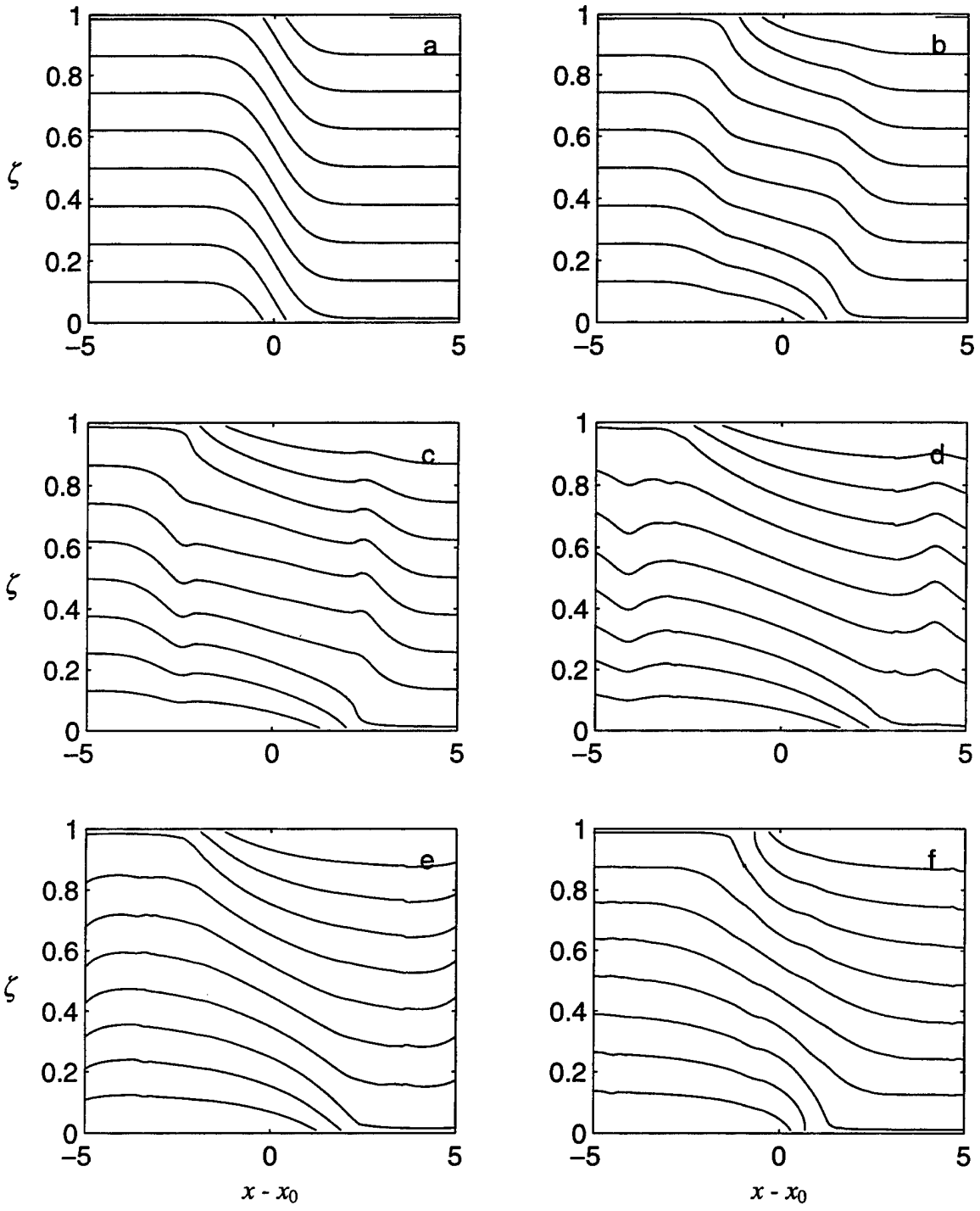

Figure 18. Time evolution of the total temperature field (point 33 in Figure 7) at (a) $t = 0$, (b) $t = 1.1f^{-1}$, (c) $t = 1.8f^{-1}$, (d) $t = 2.9f^{-1}$, (e) $t = 3.6f^{-1}$, and (f) $t = 5.0f^{-1}$.

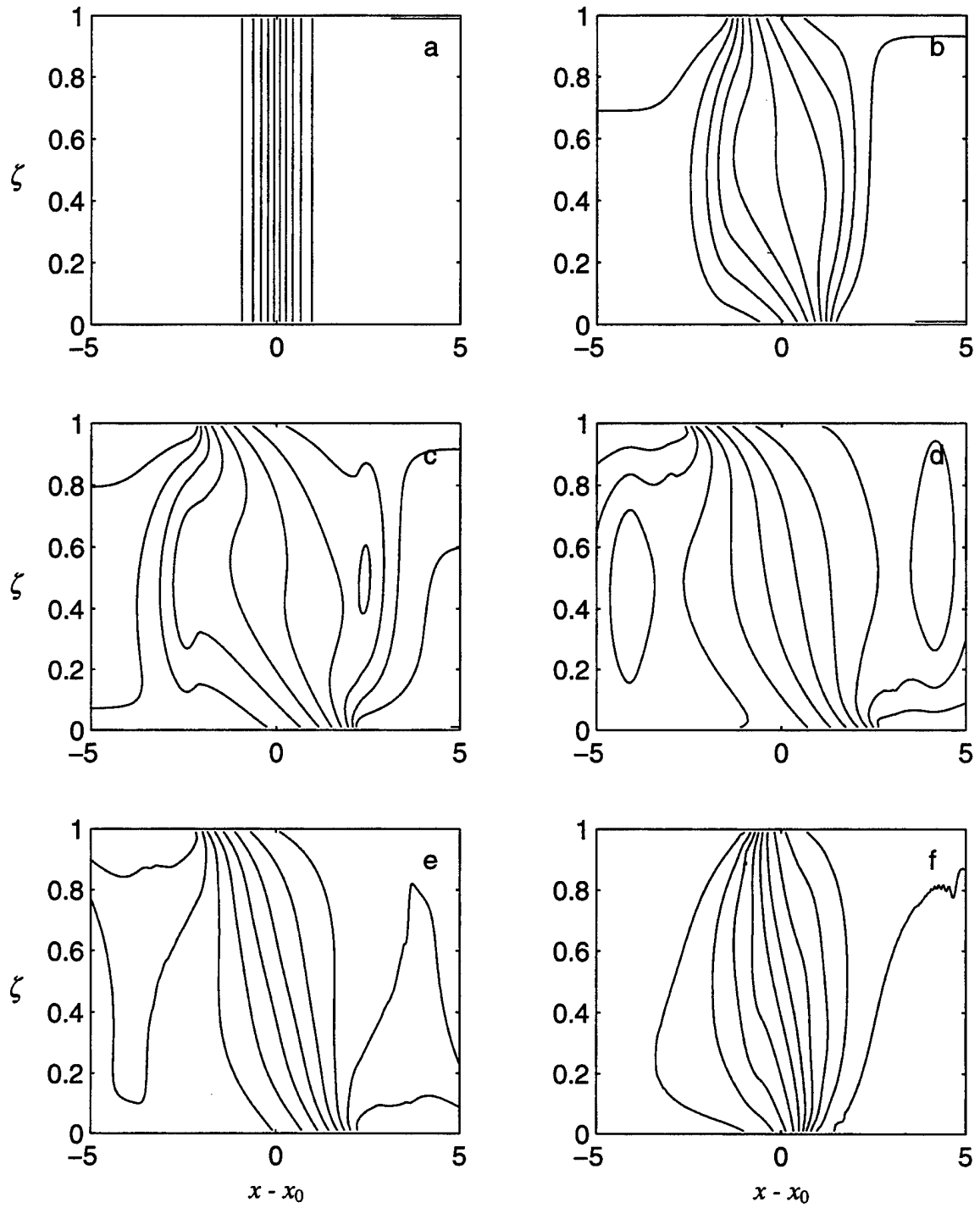

Figure 19. Same as in Figure 18, except for the temperature anomaly (removed the average value of each horizontal layer).

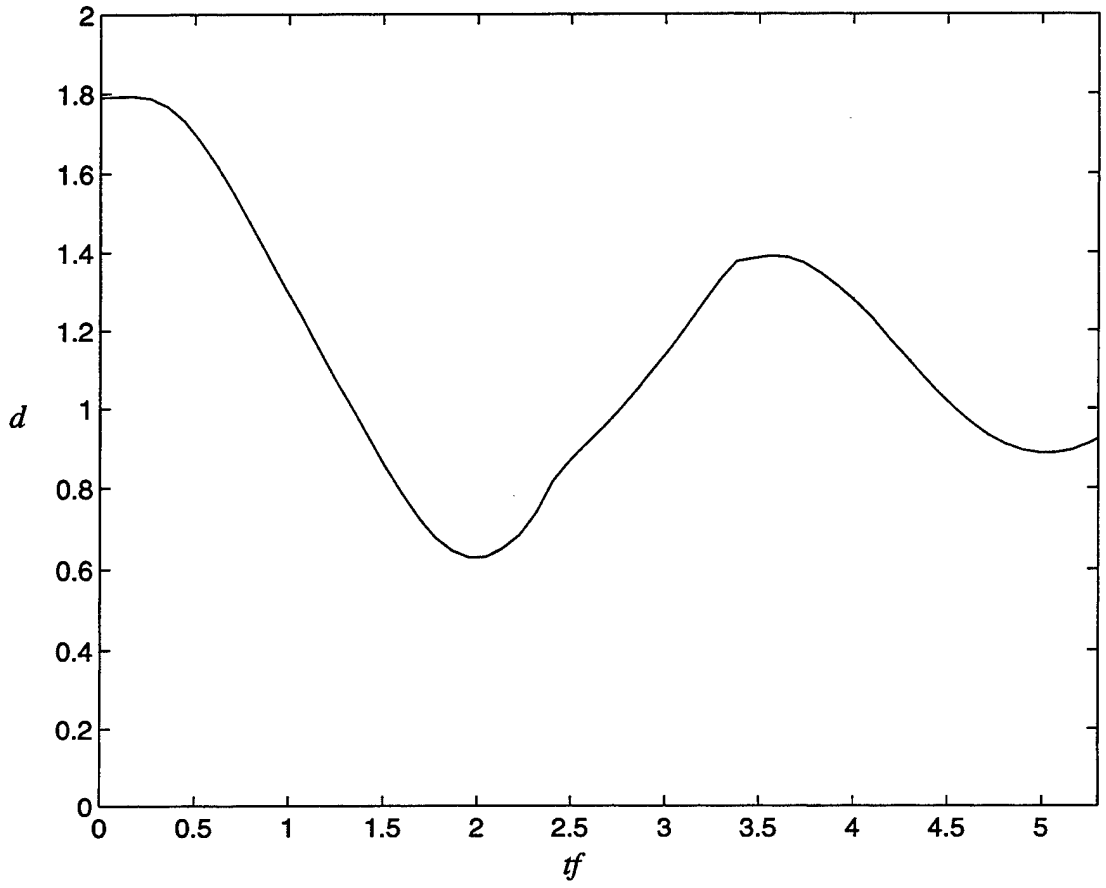

Figure 20. Time distribution of *d*-value at the lower boundary for case 33.

isotherms considerably. This distortion can mask the larger scale temperature gradient in the *d*-value calculation.

Another important difference is that the momentum field lags the mass field. Although the spatial wind distribution in this case (not shown) is similar to those in region I, the lagging is substantial. This is due to the rapid change in the temperature field by the gravity waves compared to the inertial period ($2\pi f^{-1}$). Figure 21 shows the time series for (a) *d*-value, (b) *u*, and (c) *v* in the point of maximum temperature gradient, in the lower boundary.

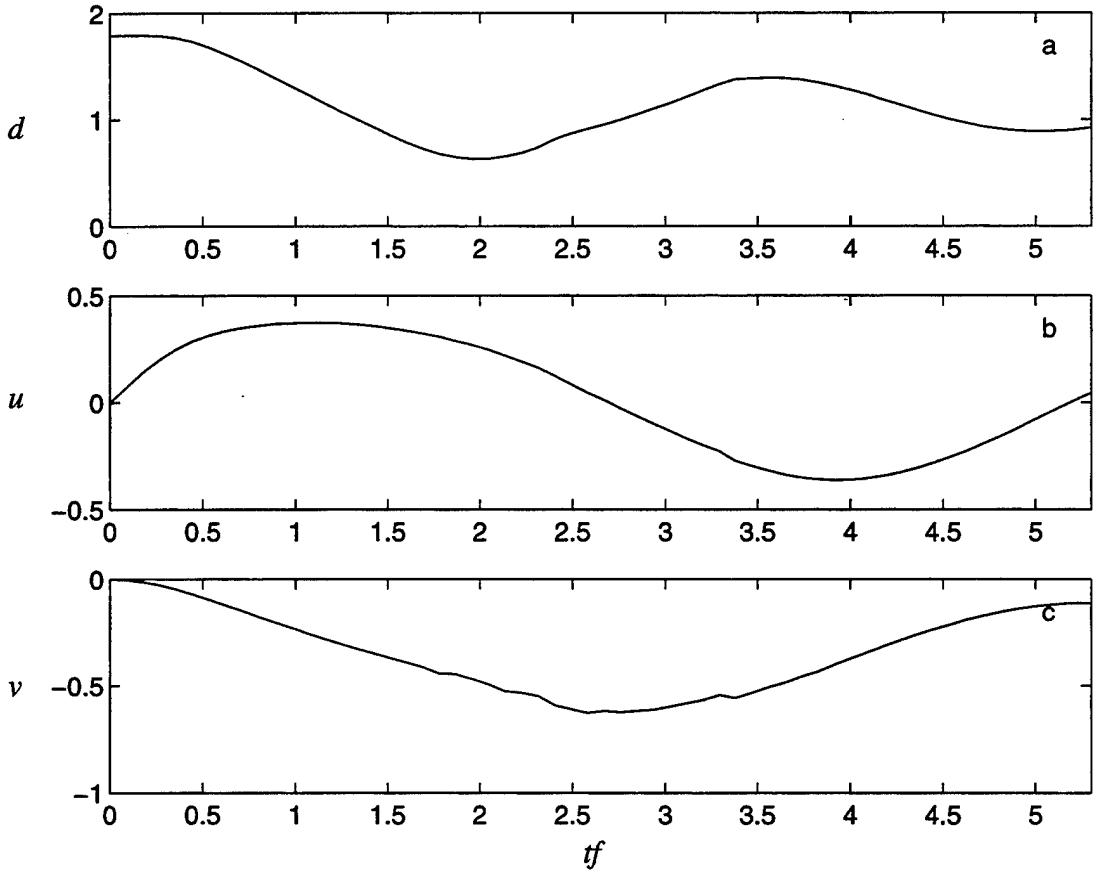

Figure 21. Time series for (a) *d*-value, (b) *u*, and (c) *v* in the point of maximum temperature gradient, in the lower boundary (point 33).

For points with larger *Ro* the period of oscillation decreases considerably compared to $2\pi f^{-1}$. The propagation speed of the fastest gravity waves increases and therefore the geostrophic adjustment process becomes much faster. As a result, the temperature gradient away from the vertical boundaries decreases faster.

D. FRONTOGENESIS WITH LARGE-SCALE ADJUSTMENT (REGION III)

The distinct characteristic for this region is the temperature collapse into a frontal zone in the upper and lower boundaries, while little change is observed away from the boundaries. The temperature anomaly at $t = 2.7f^{-1}$, in the lowest level, for case 29

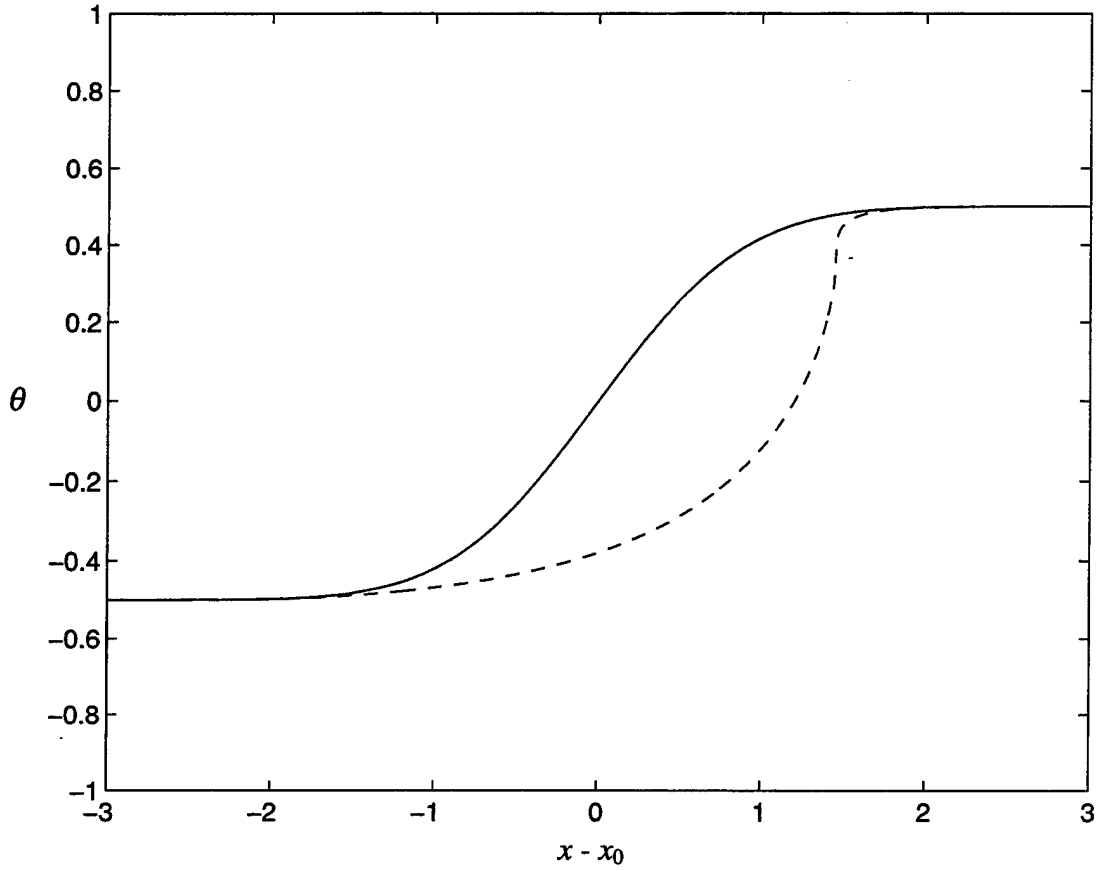

Figure 22. Temperature anomaly in the lower boundary for case 29 at $t = 2.7f^{-1}$. The frontal zone is the steep slope located at $x - x_0 = 1.5\ a_D^{-1}$.

($Ro = 1.630$ and $F = 15.302$), is depicted in Figure 22. The large temperature change in a very narrow zone characterizes the collapse, which causes the model solution to be discontinued. It can be noticed that only a fraction of the total temperature anomaly is present in the frontal region (at $x - x_0 = 1.5\ a_D^{-1}$), while the remainder goes into a very smooth gradient. The frontal zone near the surface moves rapidly toward the warmer air, causing the front to tilt toward the colder air. Figure 23 shows the d-value changes at the surface for case 29, which agrees very well with BW96. The dashed line has the

minimum grid size twice as large as the solid one. The grid size imposes a constraint on the d-value when the collapse occurs. Therefore, the minimum d-value in the first case is roughly twice that of the latter. The d-value at level $\zeta = 0.5$ (not shown) indicates very small changes in the temperature gradient at this level.

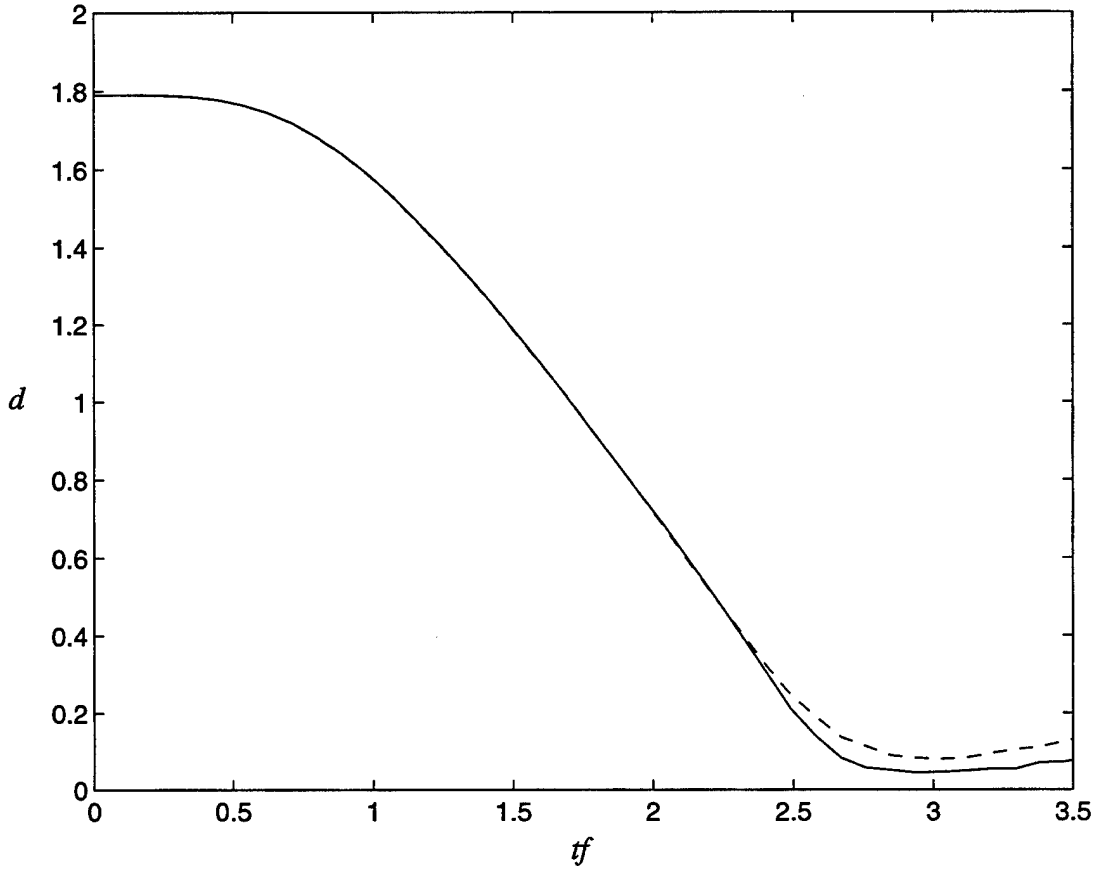

Figure 23. Time variation of the d-value for the lower boundary, for case 29. The minimum d-value is lower for the smaller grid scheme (solid line) than for the larger (dashed line). Note the fast decrease and the collapse near $t = 2.7f^{-1}$.

Figure 24 shows the evolution of the temperature anomaly field for (a) t = 0, (b) $t = 1.1\,f^{-1}$, (c) $t = 1.8\,f^{-1}$, and (d) $t = 2.7\,f^{-1}$. The momentum field for the same time is shown in Figures 25 (u component) and 26 (v component). This result is similar to the

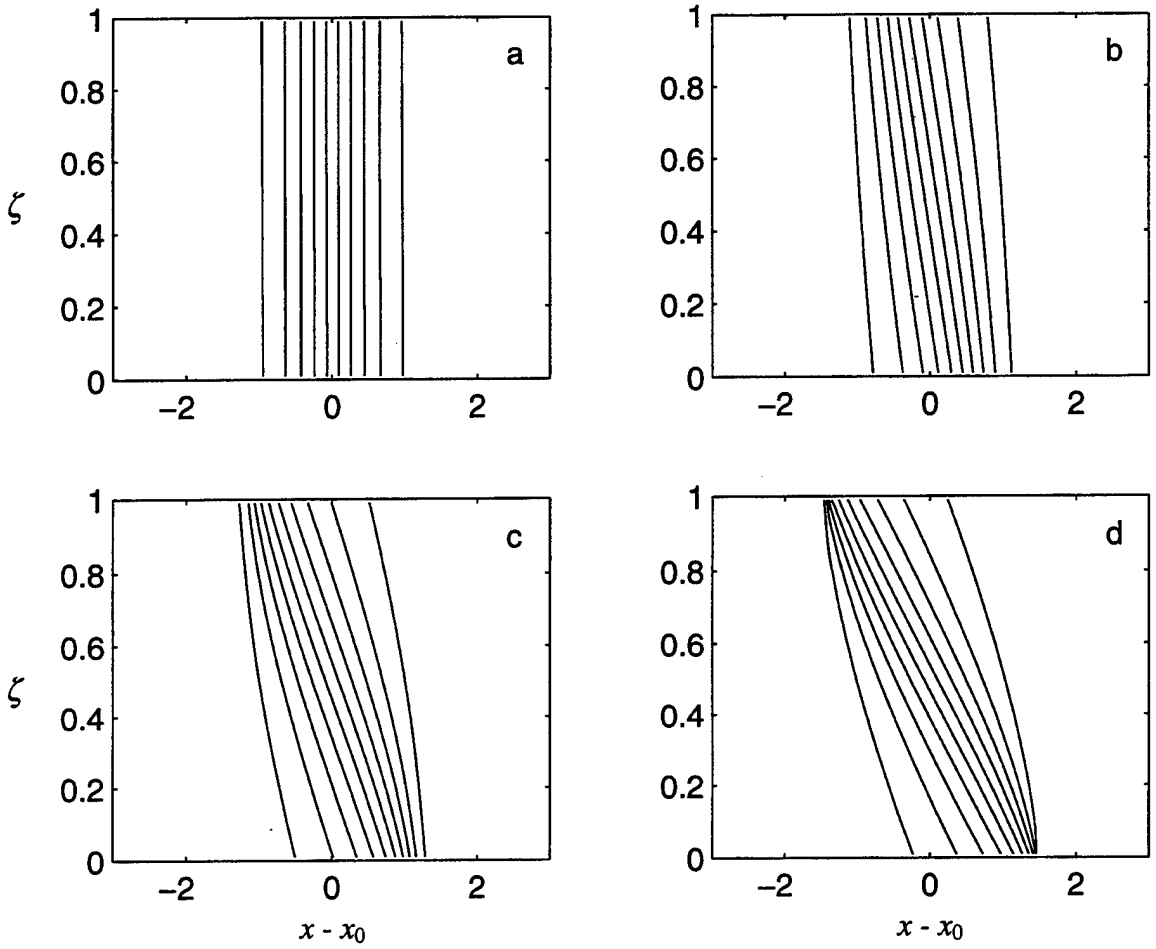

Figure 24. Time evolution of the temperature anomaly cross-section for point 29 in Figure 7, for (a) $t = 0$, (b) $t = 1.1 f^{-1}$, (c) $t = 1.8 f^{-1}$, and (d) $t = 2.7 f^{-1}$.

case showed in BW96, with $F \rightarrow \infty$. The same relationship between mass and momentum fields observed in region I also occurs in this region. The rotational component increases in phase with the gradient increase, due to the Coriolis force. The divergent component, on the other hand, increases initially because of the unbalanced pressure gradient, but is very small when the temperature collapses. This is more evident in Figure 27, which displays the time series of d-value, u and v.

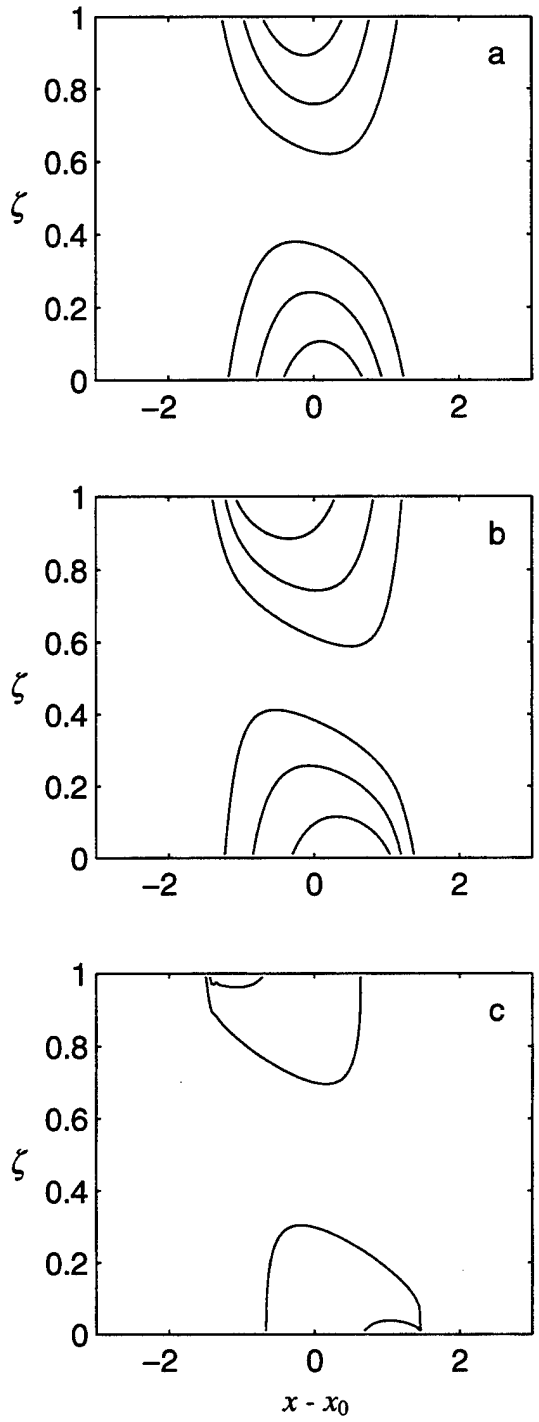

Figure 25. Time evolution of u for point 29 in Figure 7, for (a) $t = 1.1\ f^{-1}$, (b) $t = 1.8\ f^{-1}$, and (c) $t = 2.7\ f^{-1}$. The zero isoline is removed for clarity.

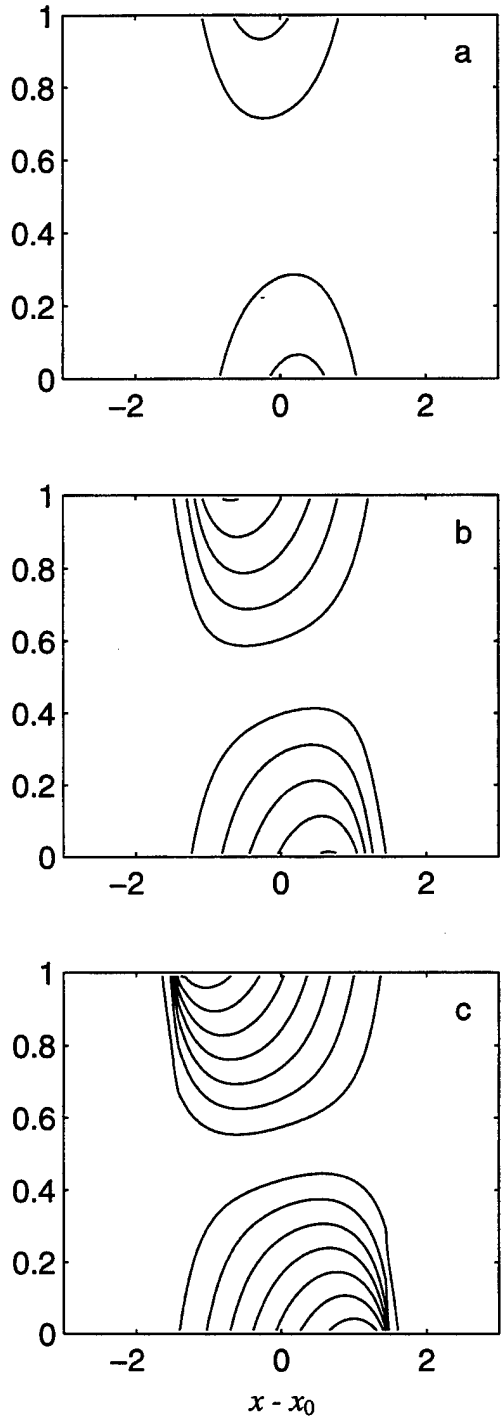

Figure 26. Time evolution of v for point 29 in Figure 7, for (a) $t = 1.1\ f^{-1}$, (b) $t = 1.8\ f^{-1}$, and (c) $t = 2.7\ f^{-1}$. The zero isoline is removed for clarity.

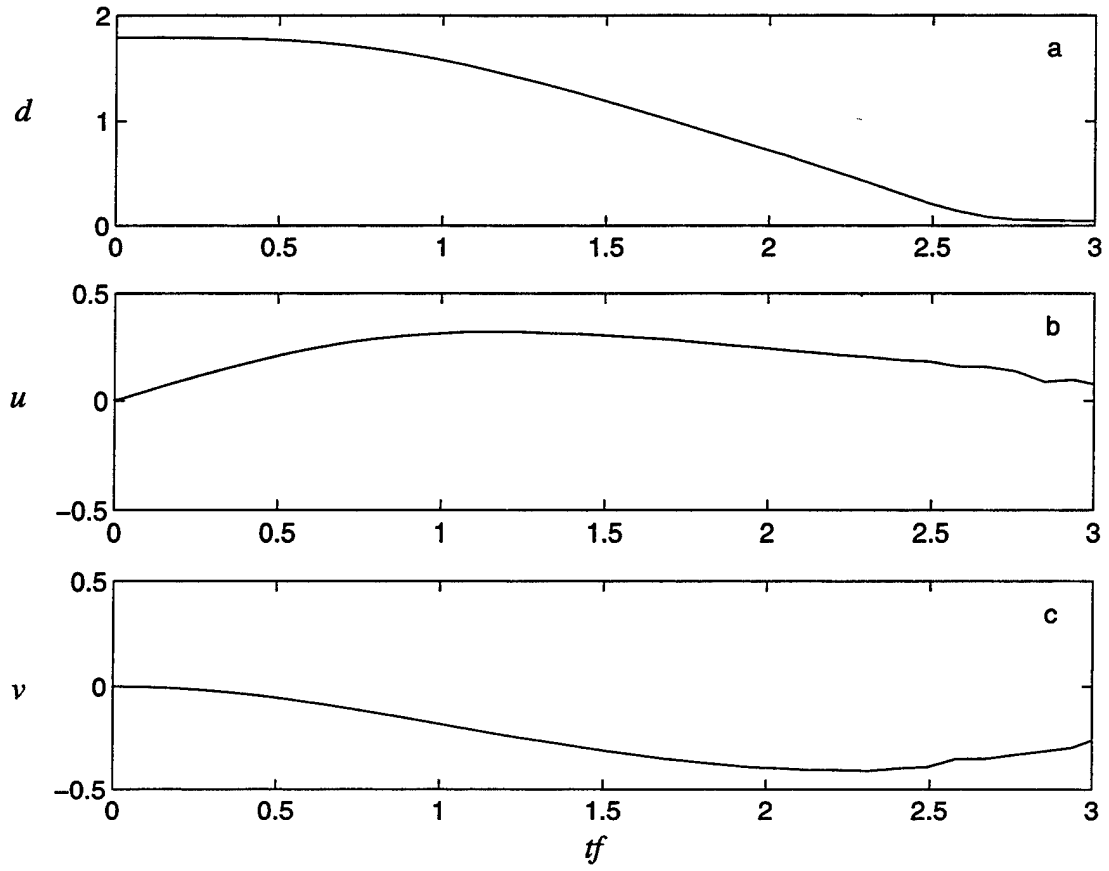

Figure 27. Time series for (a) *d*-value, (b) *u*, and (c) *v* in the point of maximum temperature gradient, in the lower boundary for case 29.

E. FRONTOGENESIS WITH SMALL-SCALE ADJUSTMENT (REGION IV)

As in region III, the temperature gradient collapses into a front but more rapidly. Figure 28 presents the *d*-value time variation for case 44 (Ro = 4.000 and $F = 0.701$), which is not different from the cases in region III, except for the time scale. Again, the dashed line represents the case where the grid spacing is twice the one in the solid line. Figure 29 shows the temperature anomaly field in the lowest level, close to the lower boundary, at $t = 1.25\, f^{-1}$. There is only part of the temperature change involved in the frontal zone as before. The main difference between this region and the previous one is

the strong damping in the mid-level temperature gradient as depicted in Figures 30 and 31.

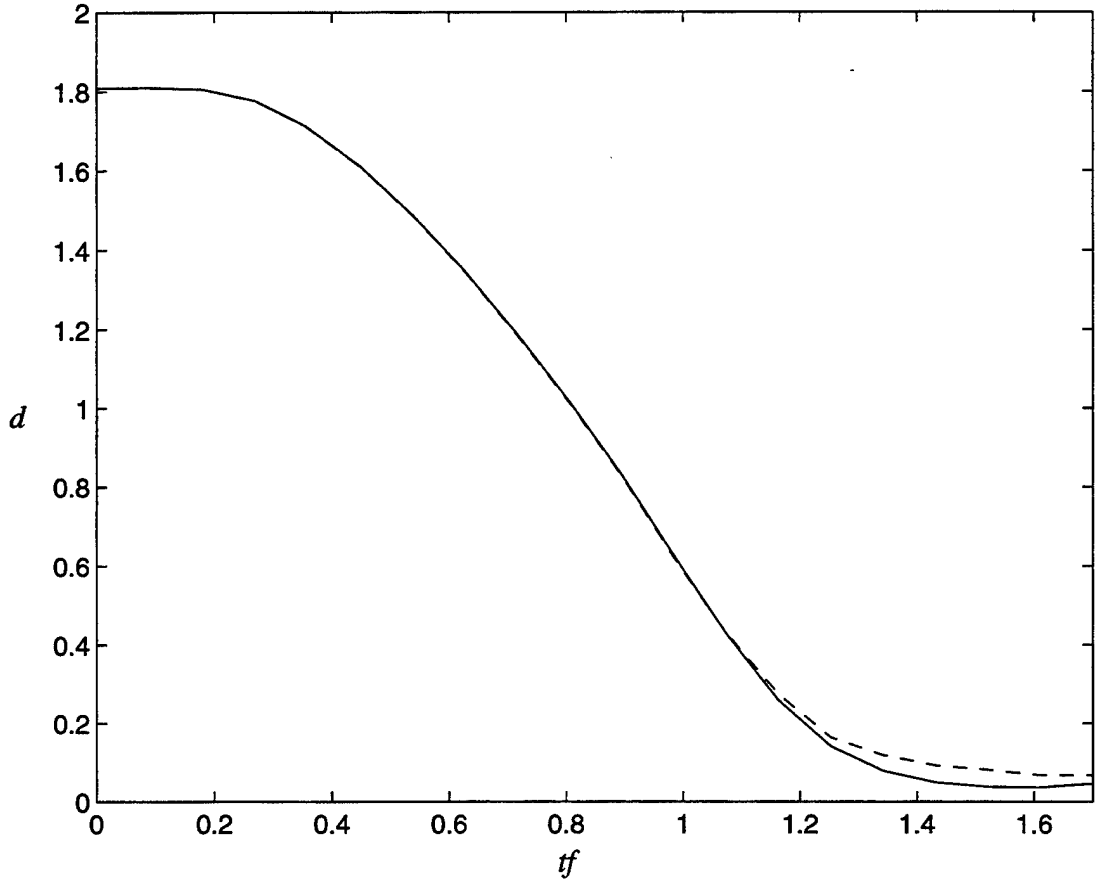

Figure 28. Time variation of the d-value for the lower boundary, for case 44. The minimum d-value is lower for the smaller grid scheme (solid line) than for the larger (dashed line). The frontal formation occurs near $t = 1.25 f^{-1}$.

The u and v fields are shown in Figures 32 and 33. Note that unlike the case in region III, the divergent wind is not negligible at the time of the frontal formation. There is a lag in the momentum field with respect to the mass field, as seen in Figure 34. This time series show the correlation and the lag between those fields.

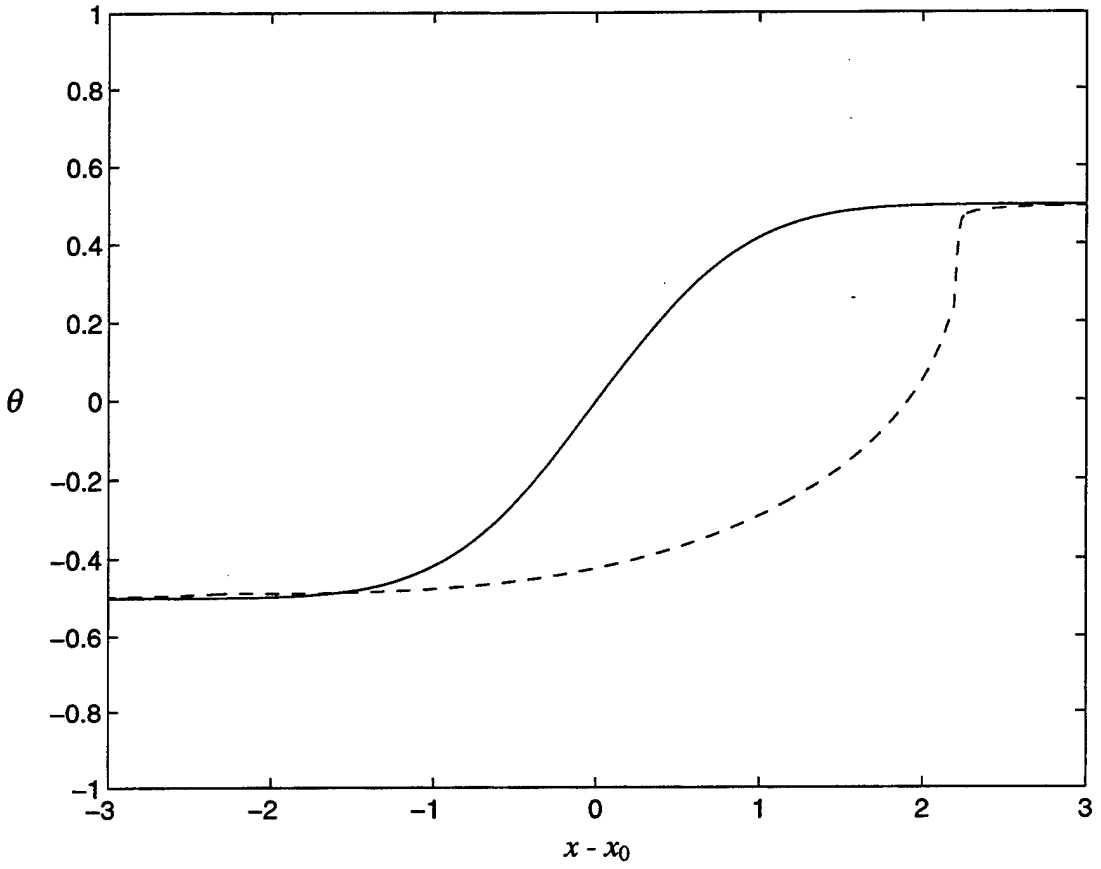

Figure 29. Temperature anomaly in the lower boundary for case 44 at $t = 1.25\, f^{-1}$. The frontal zone is located $x - x_0 = 2.2\, a_D^{-1}$.

The other cases in this region present the same behavior as case 44. A difference is the time scale involved in the frontal formation in the lower boundary. The other distinct characteristic is the geostrophic adjustment process in the midlevel zone. This adjustment is stronger for larger *Ro*.

F. TRANSITION ZONES

The transition zone between the large- and small-scale geostrophic adjustment regions is not very large. Although the cases in each region show some variation in terms of geostrophic adjustment as they approach the transition zone, this change is much more

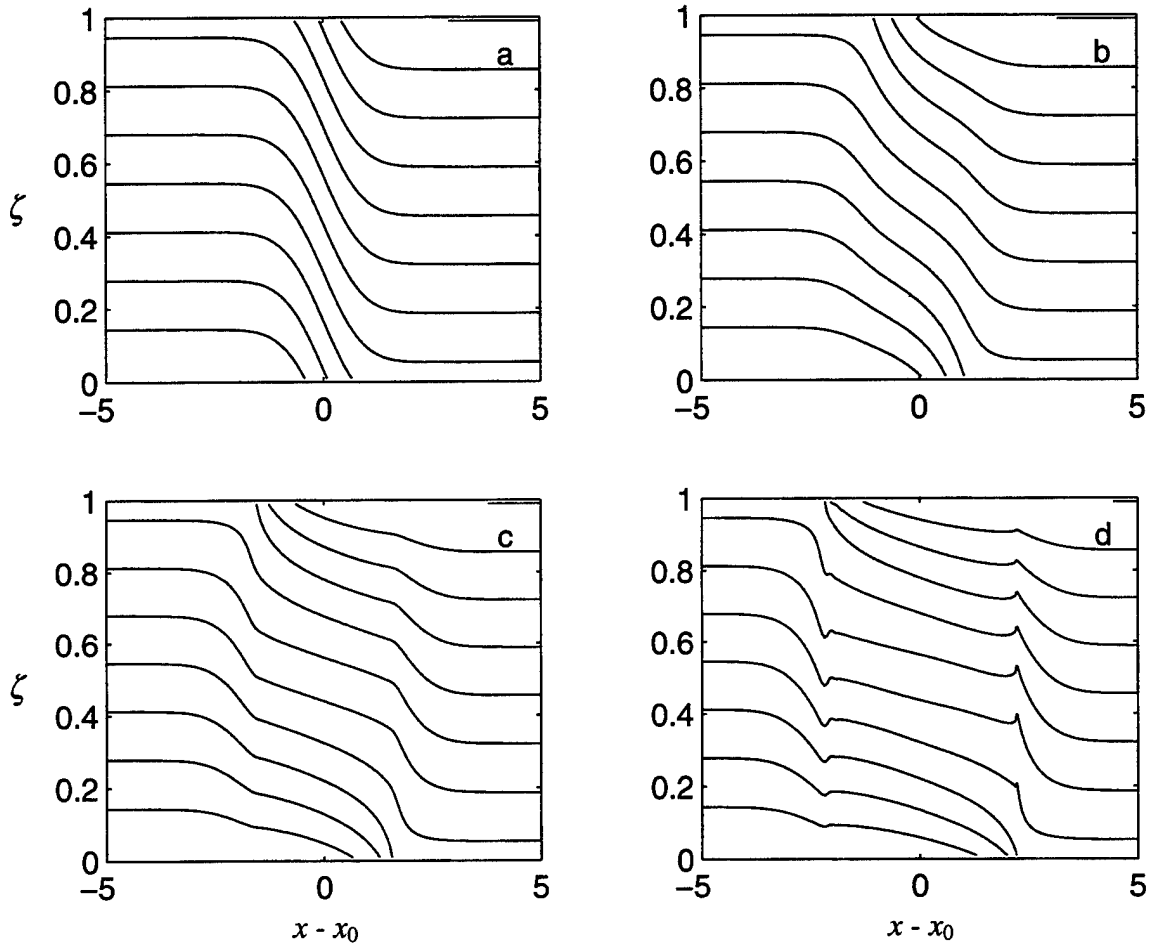

Figure 30. Time evolution of the total temperature field for point 44 in Figure 7, for (a) $t = 0$, (b) $t = 0.63 f^{-1}$, (c) $t = 0.90 f^{-1}$, and (d) $t = 1.35 f^{-1}$.

abrupt near the line $B = \pi$. This is true both when changing between regions I and II, and between III and IV. Cases 2 and 6 (see Figure 7) are located in both sides of the line $B = \pi$. They show very distinct characteristics in the mid-level temperature gradient. The former lies slightly to the right of the curve (small-scale region), and undergoes a large change in the temperature gradient as gravity waves move away from the imbalance zone. This changes are very similar to those depicted in Figures 18 and 19. The latter case is located in the region of large-scale geostrophic adjustment, and little change occurs in the

temperature gradient away from the boundaries. This behavior is analogous to the case showed in Figure 12.

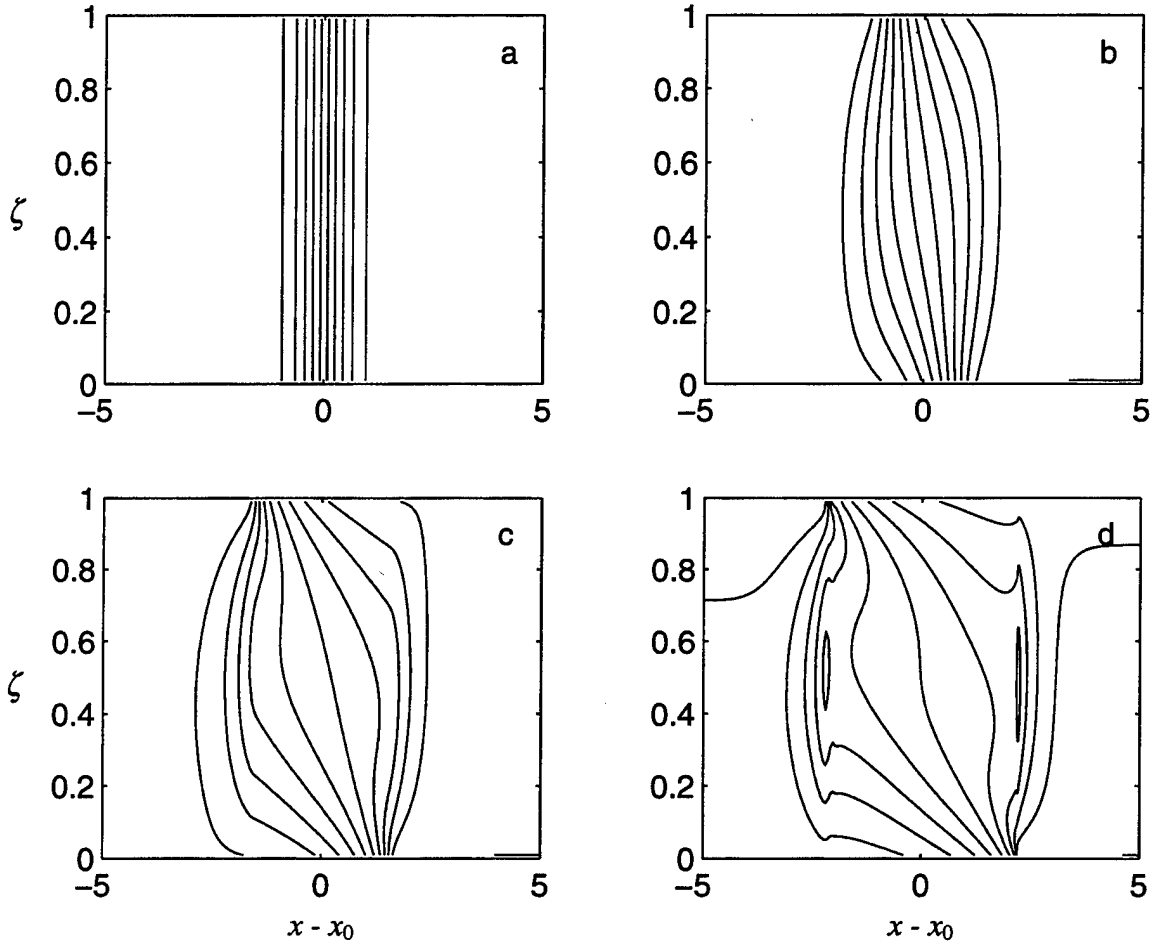

Figure 31. Same as in Figure 30, except for the temperature anomaly.

The transition from nonfrontal to frontal regions is not clear cut. The approach here is to consider that frontogenesis has occurred if all the situations below have occurred in the lowest level of the model (near the lower boundary):

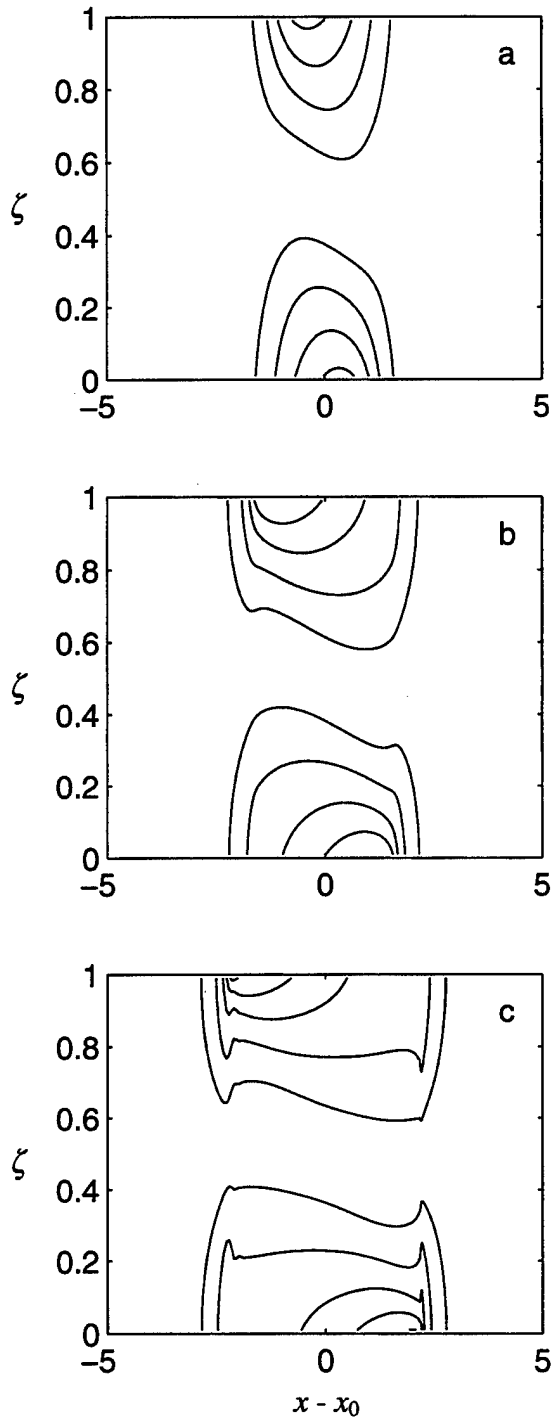

Figure 32. Time evolution of u for point 44, for (a) $t = 0.63f^{-1}$, (b) $t = 0.90f^{-1}$, and (c) $t = 1.35f^{-1}$. The zero isoline is removed for clarity.

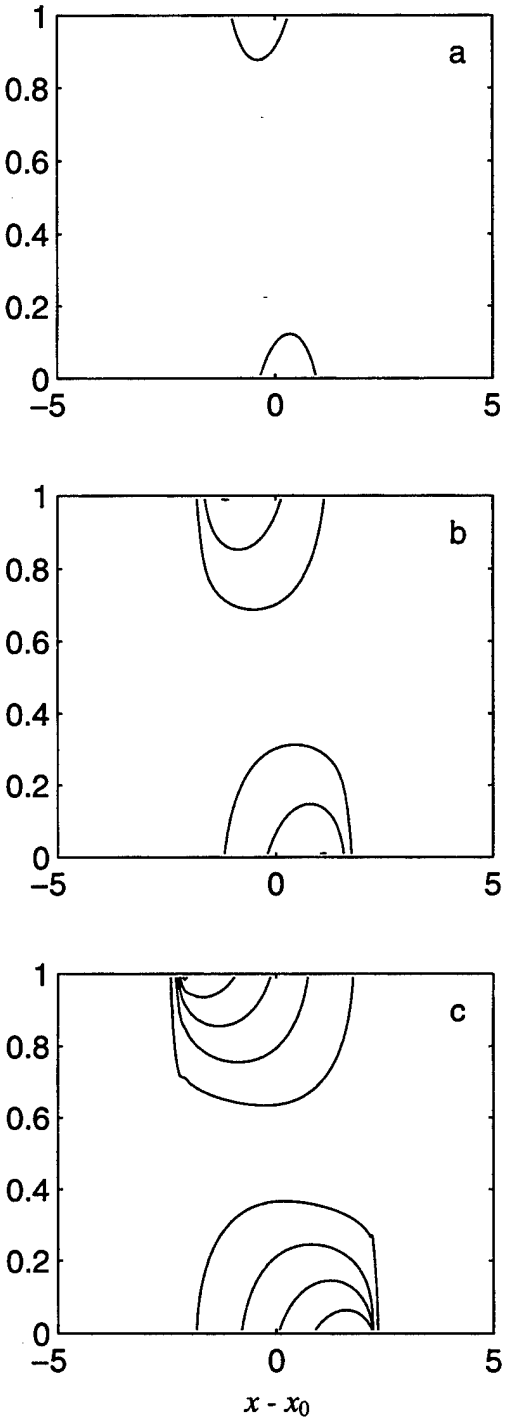

Figure 33. Time evolution of v for point 44, for (a) $t = 0.63f^{-1}$, (b) $t = 0.90f^{-1}$, and (c) $t = 1.35f^{-1}$. The zero isoline is removed for clarity.

•*d*-value at critical time is bounded by the grid size;

•*d*-value tends to zero at the critical time;

• there is no oscillation in the temperature gradient after the critical time; and

• there is a large temperature change in a few grid points.

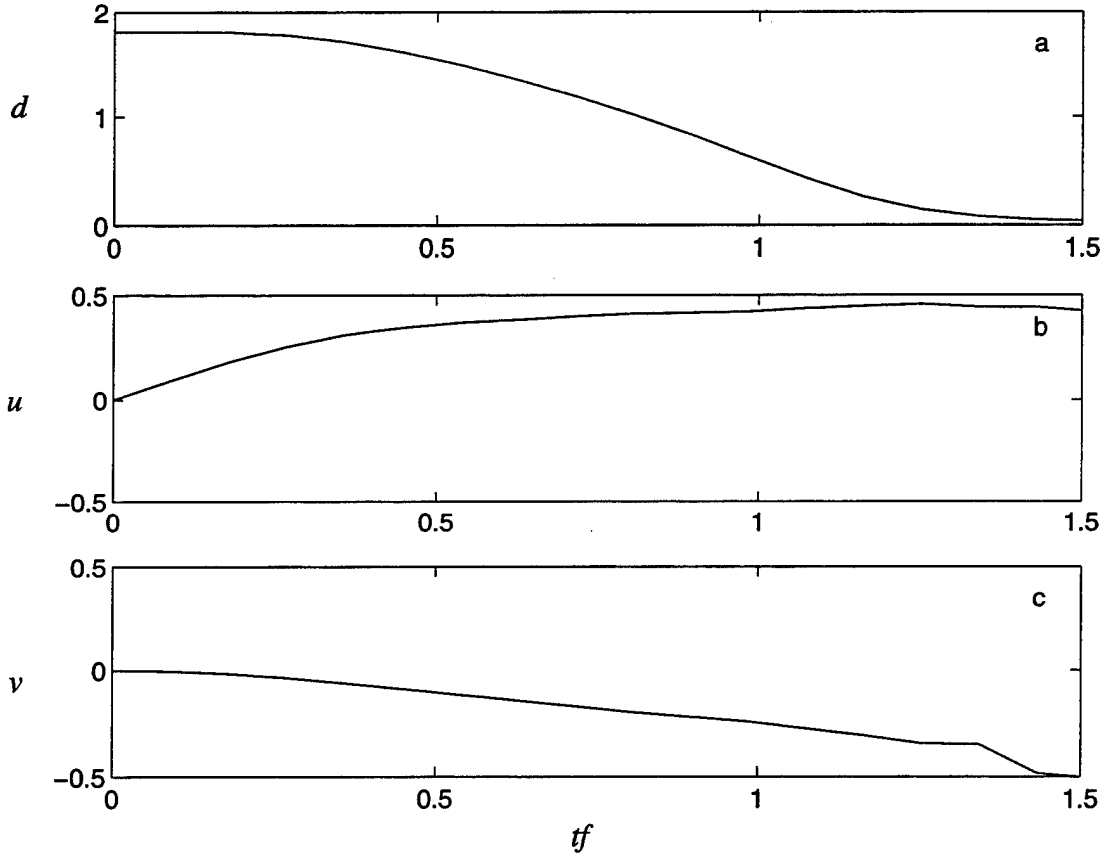

Figure 34. Time series for (a) *d*-value, (b) *u*, and (c) *v* in the point of maximum temperature gradient, in the lower boundary for case 44.

The first criteria is evaluated by comparing the *d*-value for a given characteristic flow (*Ro*, *F*), run with two different grid spacings. Figure 35 presents the *d*-value for $\Delta x = 0.01$ (dashed) and $\Delta x = 0.005$ (solid), for case 20. The ratio of the two Δx is 1:2

while the ratio of the d-values is 1:1.7. This is very close considering that finite difference models have different precision for different Δx and that this is a non-linear model. However, not all the change in temperature is in the frontal zone and thus the ratio between the different Δx is not a precise measurement of the ratio between the two d-values. Nine cases were found to be in this transition zone. The average ratio of d-value is 1:1.6 with a standard deviation of 6%.

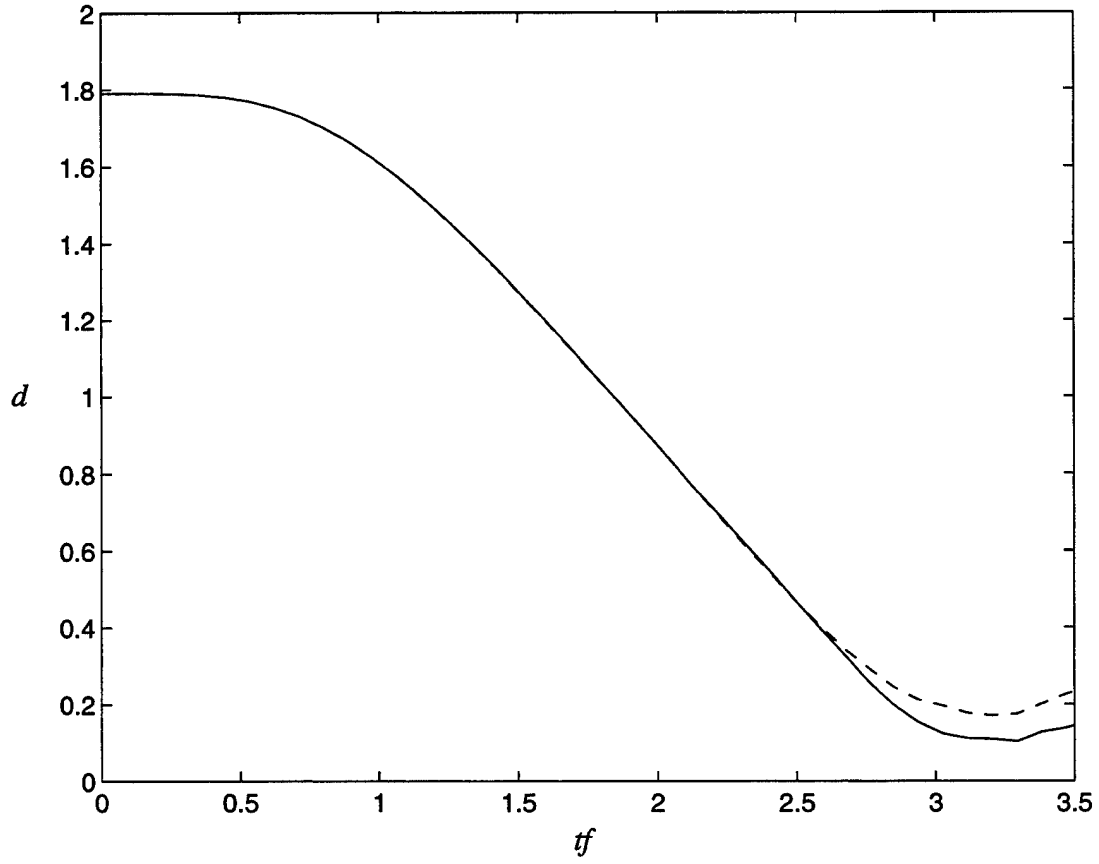

Figure 35. Time evolution of d-value for case 20 for $\Delta x = 0.01$ (dashed) and $\Delta x = 0.005$ (solid). The front collapses near $t = \pi f^{-1}$.

Model runs have shown that $d \cong 0.10$ marks the beginning of the frontal region. There is no frontal formation when $d > 0.10$ and a front has formed when $d \leq 0.10$. Analysis of case 20 ($Ro = 1.543$ and $F = 7.999$) shows a good consistency with the above characteristics. It is located between a nonfrontal and a frontal case and has a minimum $d = 0.10$ which is much smaller than the initial d-value. It is important to notice that this limiting $d \cong 20\ \Delta x$ and for stronger frontal cases $d \rightarrow \Delta x$.

The frontal formation causes the collapse of the temperature gradient and thus interrupts the oscillation observed in nonfrontal cases, which leads to the third criteria. It can be seen in Figure 35 that the temperature gradient in case 20 does not oscillate as in a nonfrontal situation. After the temperature collapse, there is no meaningful numerical solution and the model output is discontinued. The last criteria consists in observing how close the temperature distribution resembles the ideal case shown in Figure 3. The temperature distribution in the lowest level of the model is shown in Figure 36 (case 20). The circles represent the grid points and indicate the number of grid spaces that are involved in the temperature jump. This jump usually happens in three to four grid spaces, which is a rather small frontal zone with horizontal scale of $O(0.02a_D^{-1})$ for the smaller grid spacing and $O(0.04a_D^{-1})$ for the larger one. It is important to notice that the scale continues to fall as long as Δx is decreased.

An empirical exponential-type curve that establishes the limit for frontal formation is presented in Figure 37. This limit is defined by the following relation between Ro and F:

$$F = ae^{-b(Ro-c)^d} + e, \tag{41}$$

where $a = 25.0$, $b = 3.90$, $c = 1.53$, $d = 0.23$, and $e = 0.37$. Frontogenesis occurs for F larger than the RHS of (41). An important characteristic is the asymptotic convergence to $Ro = 1.53$. The lower part of the curve shows the tendency for asymptotic convergence to a limiting F. To evaluate the convergence for larger Ro it would be necessary to use a finer resolution model with larger domain. The stability increases excessively and causes the gravity waves to propagate very fast. As a result, the front also moves very fast and requires a larger zone with finer resolution. The domain must be increased so that the gravity waves will not reach the lateral boundaries. The curve seems to converge to a value close to $F = 0.37$.

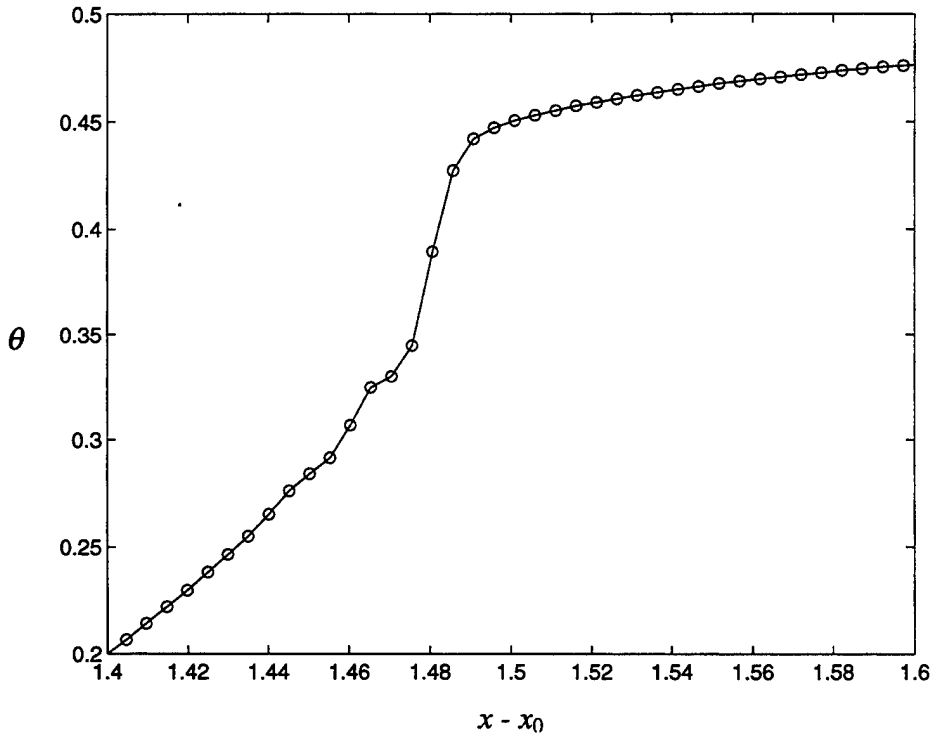

Figure 36. Temperature distribution in the lowest level of the model for case 20. The circles represent the grid points. The jump occurs in few grid points.

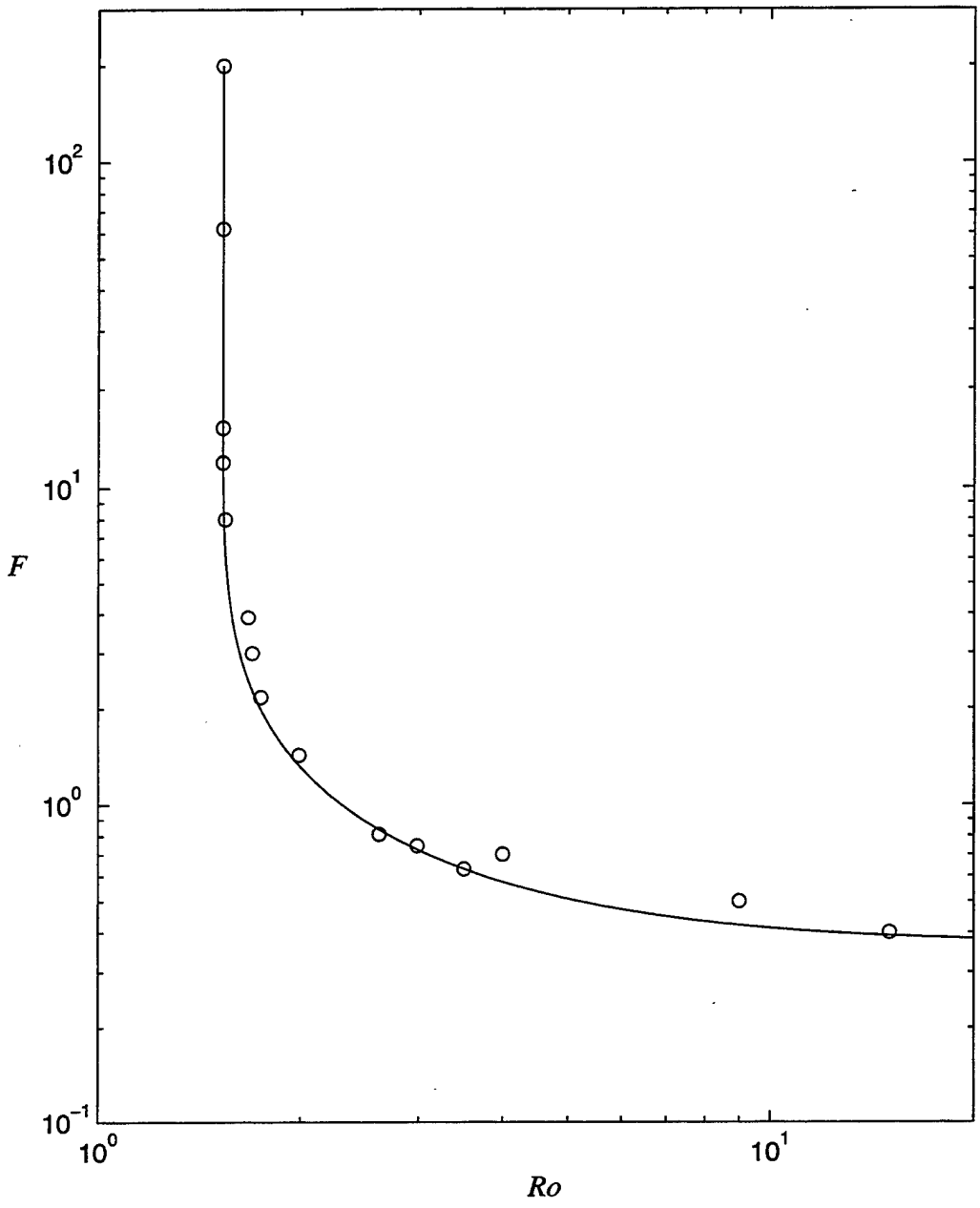

Figure 37. Limit of the frontal and nonfrontal formation as defined by equation (41) in a log-log plot. Frontogenesis occurs in the concave side of the curve. The curve asymptotically converges to $Ro = 1.53$. It also seems to converge to $F = 0.37$ for large Ro, although not as clear as for the large F convergence. The circles are the cases used to establish the curve. The points closer to the curve have d closer to 0.1.

G. ZERO PLANETARY VORTICITY

The planetary vorticity (f) is very important for small Ro as seen in sections B and D. The period of oscillation of the temperature gradient is nearly inertial ($2\pi f^{-1}$). As Ro increases, however, the oscillation departs from the inertial value, as in sections C and E. For large values of Ro, the planetary vorticity plays a very small role. Case 57 (see Figure 7) has $Ro = 9$ and $F = 0.5$, and was integrated using $f = 10^{-4}\text{s}^{-1}$. It is compared to a similar case with $f = 10^{-8}\ \text{s}^{-1}$ ($Ro \rightarrow \infty$). Figure 38 displays the time evolution of the d-value for $f = 10^{-4}\ \text{s}^{-1}$ (solid line), and $f = 10^{-8}$ (dashed line), where the horizontal axis is

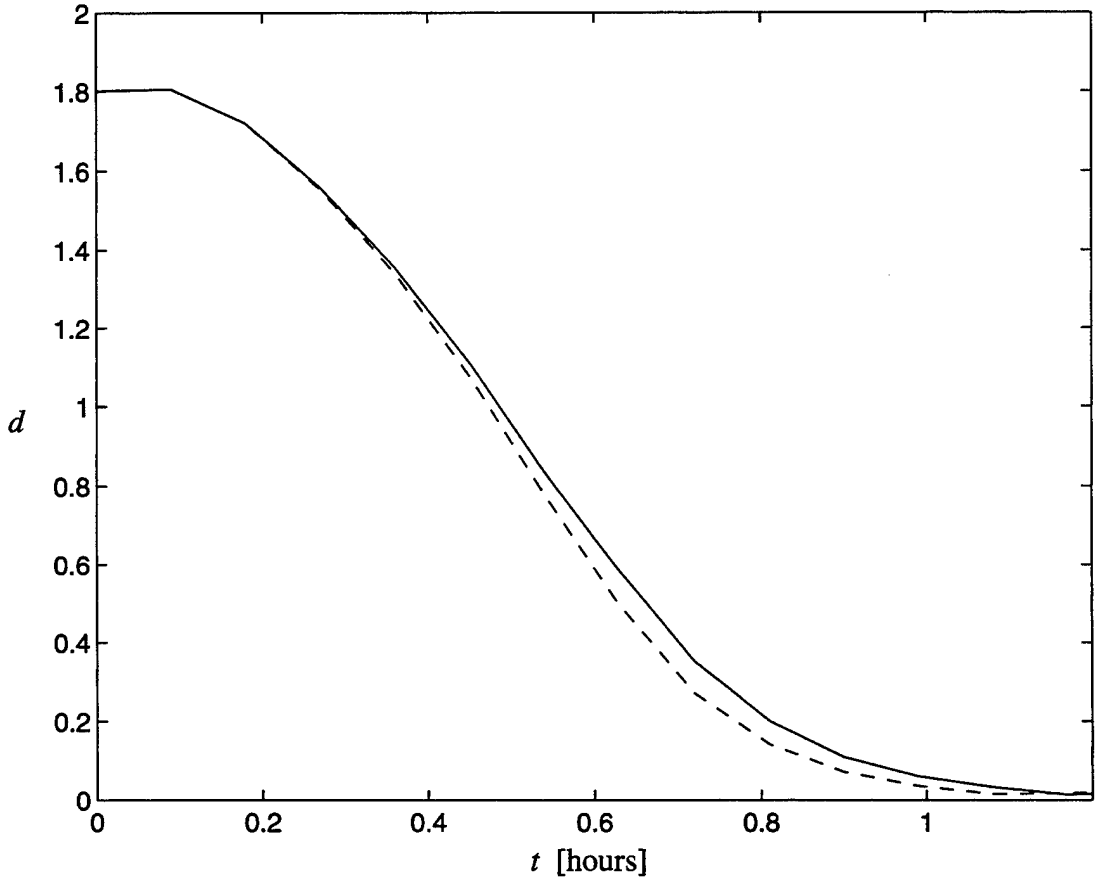

Figure 38. d-value evolution for $f = 10^{-4}\ \text{s}^{-1}$ (solid line), and $f = 10^{-8}\ \text{s}^{-1}$ (dashed line). The former slightly lags the latter.

the dimensional time (in hours). The two curves start at the same point and slightly separate, beginning at $t = 0.3$ hs. Although the absence of planetary vorticity causes the front to form a little earlier than the nonzero case, the θ and u fields behave similarly in both situations. The two cases are different because Ro is not large enough in the former case and $Ro \rightarrow \infty$ as $f \rightarrow 0$. This case is also treated for $F \rightarrow \infty$ in studies by Simpson and Linden (1989) and Kay (1992).

The temperature and divergent wind component fields for this two cases, close to the time of frontal formation (not displayed), show very subtle differences. The only significant difference for large Ro atmosphere is in the rotational wind component. There is no thermal wind balance due to the lack of planetary vorticity. Therefore, the rotational part of the wind is zero when $f \rightarrow 0$.

VI. DISCUSSION

The geostrophic adjustment using the present model is very consistent, and it happens in the levels where the influence of the upper and lower boundaries is small. The initial unbalanced state excites gravity waves that propagate away from the imbalance region, for a very large domain. The mass and momentum fields tend to a geostrophic balance as the divergent field vanishes. During the geostrophic adjustment process, the temperature and the wind fields oscillate about the steady state solution, as the gravity waves propagate away from the imbalance region.

A limit between the large-scale ($a_D^{-1} > L_R$) and small-scale ($a_D^{-1} < L_R$) geostrophic adjustment regimes is set by $B = \pi$. Therefore $B > \pi$ leads to an adjustment that depends on the initial wind field (small-scale process), and $B < \pi$ depends on the initial mass field (large-scale process). The transition zone between the two regimes is small, as discussed in chapter V, section F. In the type of initial state here presented, large-scale regime tends to have small changes in the temperature gradient in the levels distant from the vertical boundaries, except for the tilting of the isothermals. When $F \rightarrow \infty$, there is just the inertial oscillation. In the small-scale regime, on the other hand, the fields tend to a state of no temperature gradient and no motion, because the initial state is at rest. If an initial imbalance consisted of a uniform horizontal temperature field and a nonzero wind field, the geostrophic adjustment would lead to a different final state. The large-scale final state would be zero and the small-scale final state would consist of a temperature field in thermal wind balance with the rotational wind field.

The temperature gradients in the lower and upper boundaries are not driven by the Rossby radius of deformation (L_R). The temperature behavior near the vertical boundaries is independent of B/π. Rather, the temperature change depends on the intensity of the divergent part of the wind. Convergence near the maximum temperature gradient is required for further intensification. The intensity of the divergent wind is a function of the initial state of the atmosphere, as defined by the pair (Ro, F). A proposed limit for frontal formation is defined by the curve presented in Figure 37. It differs from Blumen's curve mainly for large Ro. Figure 39 displays both curves in a log-log plot. The curve suggested in this work (solid line) seems to converge to a limiting $F = 0.37$. Blumen's curve (dashed line) suggests the convergence would occur to a smaller Froude number and not so rapidly.

Near the upper and lower boundaries, the temperature gradient also oscillates when a front does not occur. The period of oscillation (T) is nearly inertial. For points distant from the limiting curve, with no frontal formation, the model is nearly linear and the d-value oscillates smoothly with the fundamental period of oscillation. For points closer to the curve, however, the nonlinear effects cause high frequency oscillations superimposed on the fundamental frequency and the d-value is no longer smooth. Figure 40 presents the time evolution of the temperature gradient for cases 1 (Ro = 2.215, F = 0.685) and 2 (Ro = 2.476, F = 0.765), the latter being closer to the limiting curve. Case 1 oscillates smoothly while case 2 contains high frequency oscillations. Figure 41 shows the calculated d-value variation for case 36 (large F), as well as the distribution

after filtering frequencies greater than $2\pi f^{-1}$, with a Chebychev filter. The dashed lines represent the analytic solution for that case, whose period is $2\pi f^{-1}$.

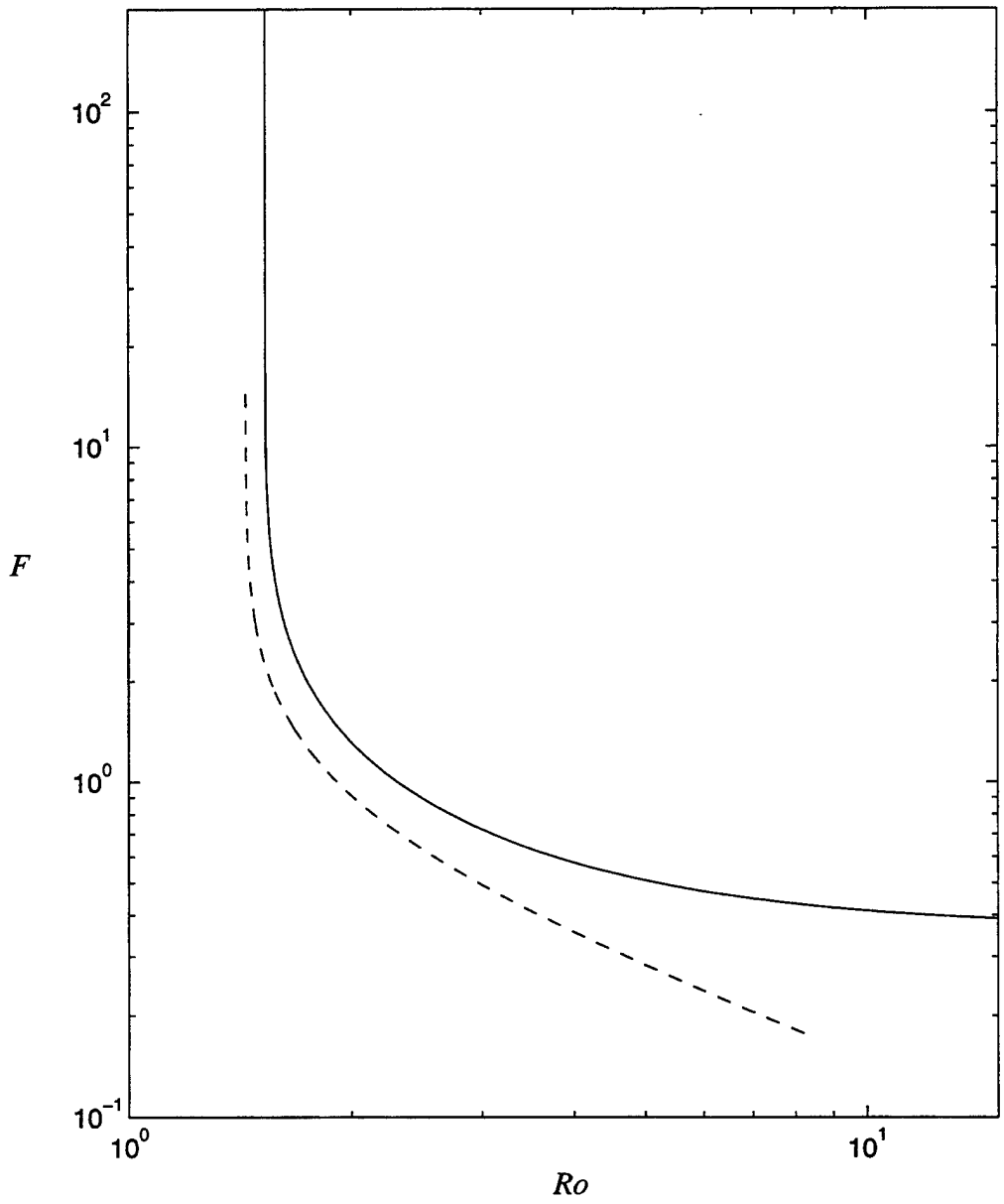

Figure 39. Limiting curves for frontogenesis as proposed by Blumen (dashed line) and by this study (solid line). The difference increases with *Ro*.

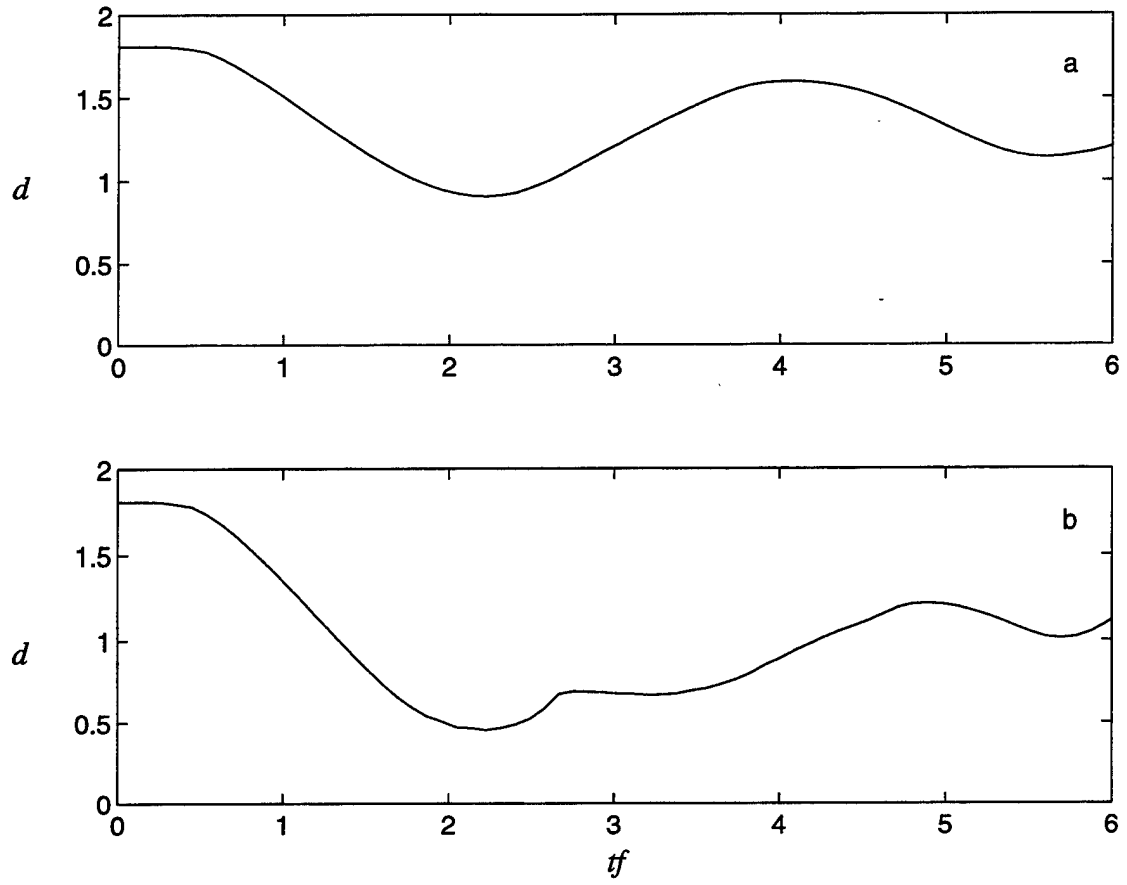

Figure 40. Time evolution of the temperature gradient (d-value) for cases (a) 1, and (b) 2. Case 2 is significantly modified by the nonlinear terms.

The fundamental period of oscillation is not constant for all situations, and seems to depend on Ro, F and N. For $Ro < 1.53$ (the limiting Rossby number), the oscillation is inertial and $T = 2\pi f^{-1}$. The period of oscillation changes for $Ro \geq 1.53$, as shown in Figure 42, where the horizontal axis is Ro/F and the vertical is NT. The curve seems to fit all the cases except the ones located below the limiting F (not shown), because of the very high stability. The half-period of oscillation was assumed to be the time the d-value takes to achieve its first minimum, starting at the origin.

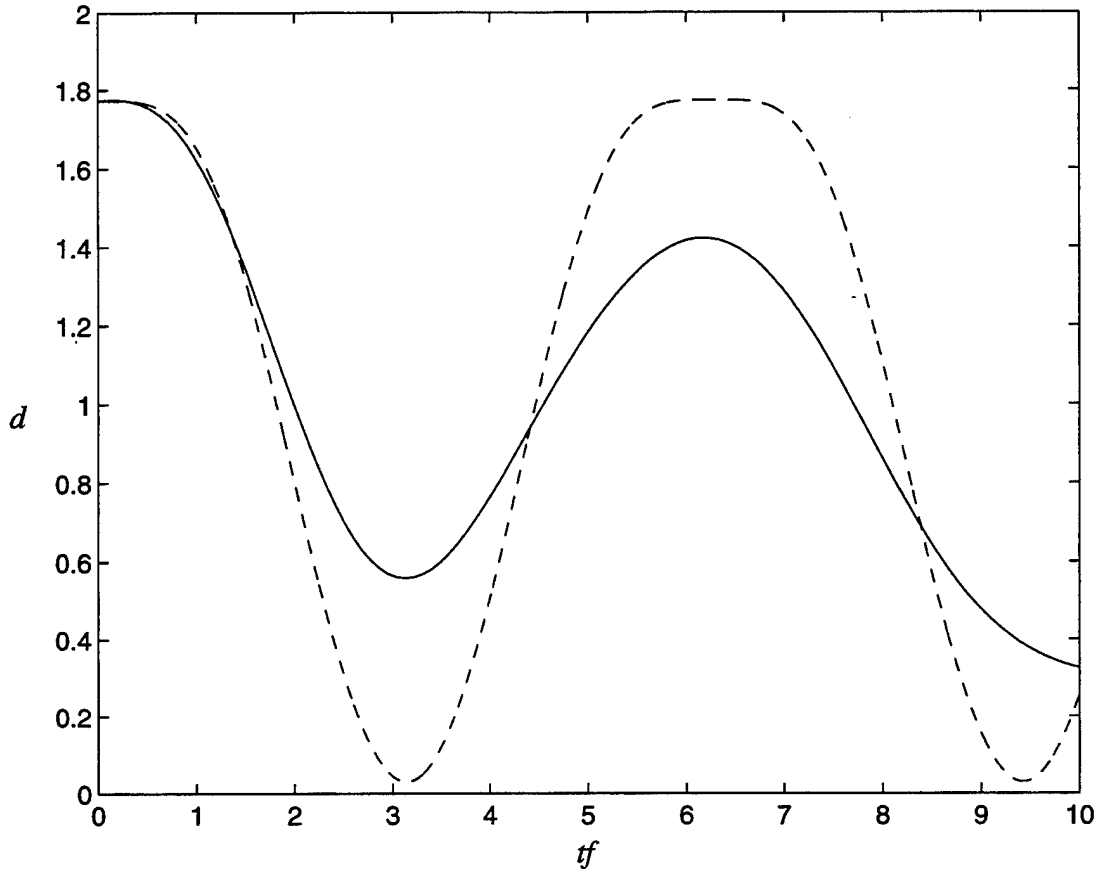

Figure 41. *d*-value variation for case 36 with (a) regular calculation, and (b) after filtering frequencies higher than the inertial frequency, using a Chebychev filter.

When the pair (*Ro*, *F*) is located over or in the concave side of the limiting curve, the temperature gradient no longer oscillates. A jump discontinuity forms which characterizes frontogenesis. The time (t_a) for a front to form in a zero potential vorticity atmosphere can be calculated with the help of equations (35) and (36). These equations do not consider the barotropic pressure gradient and were derived for the zero potential vorticity case. The barotropic term is not significant for strong forcing associated with frontal formation and becomes less important form stronger cases (BW96). As a result, larger *Ro* fluids tend to have smaller difference between the analytic (t_a) and the

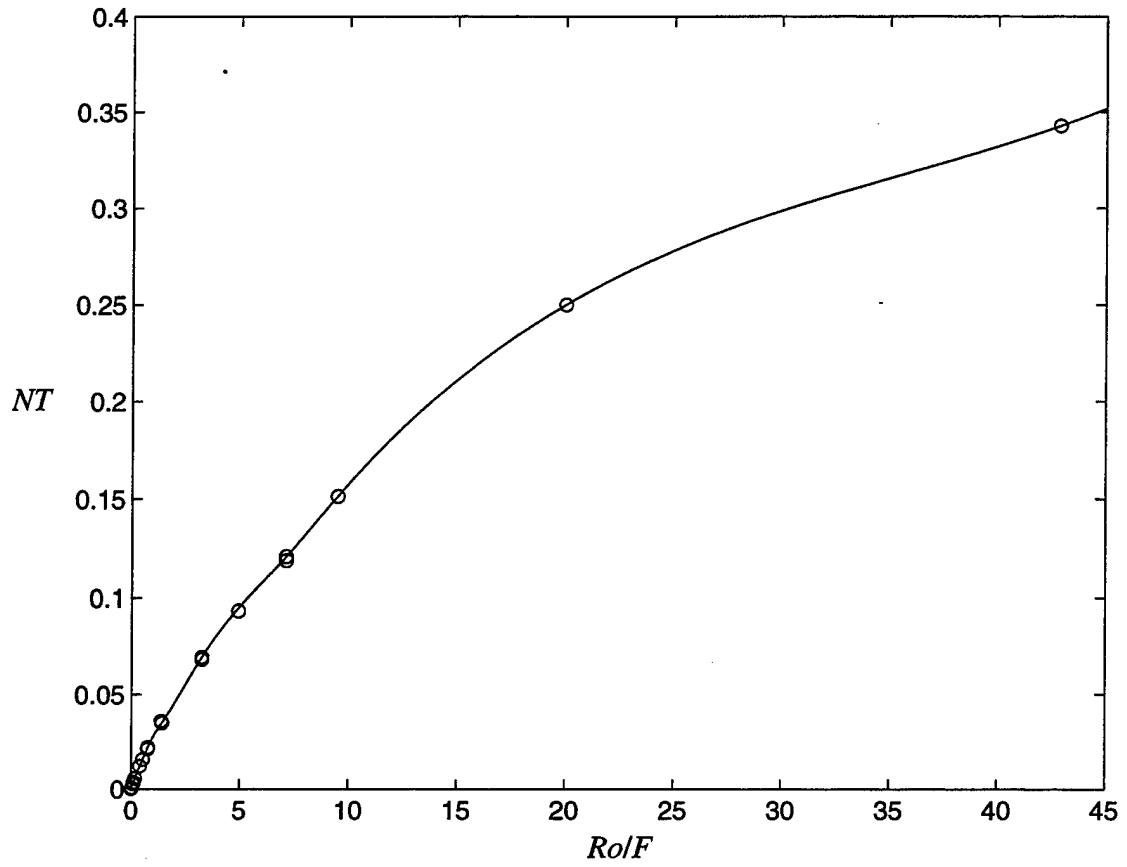

Figure 42. Variation of the oscillation period with *Ro*, *F*, and *N*, for $Ro \geq 1.53$, and $F > 0.37$. These cases (circles) do not produce fronts and oscillates with period *T*. The solid line is a cubic spline interpolation for those points.

actual time (t_c) for a front to form. However, for nonzero potential vorticity situations, this relationship is not so straightforward. Stronger fronts form much more rapidly than weaker ones. In this study, the time frontogenesis occurs is considered the intercept of the extrapolation of the almost linear part of the *d*-value curve with the time axis, as presented in Figure 43 (for case 22). This procedure is more consistent with the analytical solution, as presented in Figure 4, and it avoids the change in the slope of *d* caused by using a discretized domain. The ratio t_a/t_c decreases when *F* decreases but also decreases for weaker frontal cases. This means that the ratio is larger for points located far from the

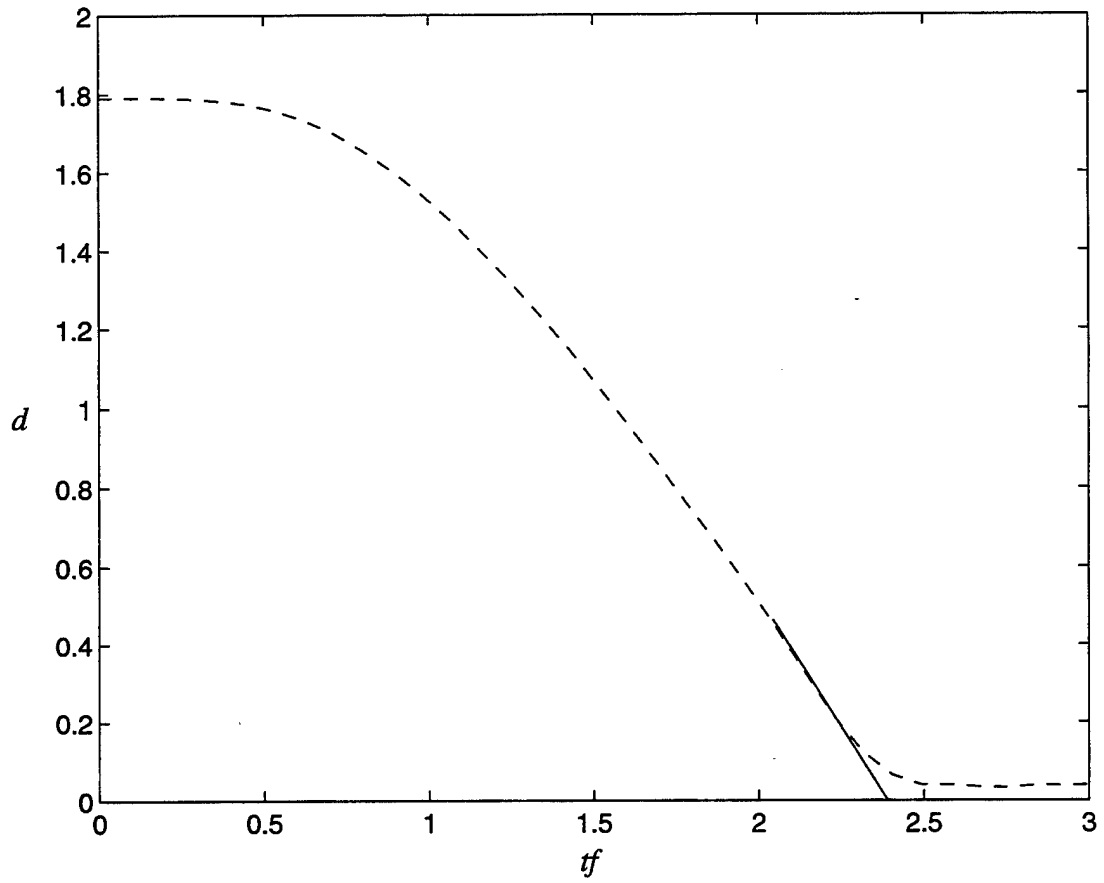

Figure 43. The time for a front to occur is obtained by extrapolating the almost linear part of the d-value curve until it intercepts the time axis. In this case, a front is considered to form at $t = 2.39f^{-1}$.

limiting curve (in the concave region). Figure 44 presents the ratio t_a/t_c as a function of F^{-1} for the cases analyzed in this work. The crosses represent the cases with $8 \leq d < 12$ (weak frontogenesis) and the circles, $d < 8$ (strong frontogenesis). The solid line is a second order polynomial fit for the weak cases. The points along the limiting (Ro, F), marked with crosses, put a lower bound for the t_a/t_c ratio. Stronger frontogenetical cases depart from this lower limit as the barotropic pressure gradient becomes less important.

Another important characteristic of the frontal temperature distribution is the relatively small amount of the total temperature change involved in the jump. The

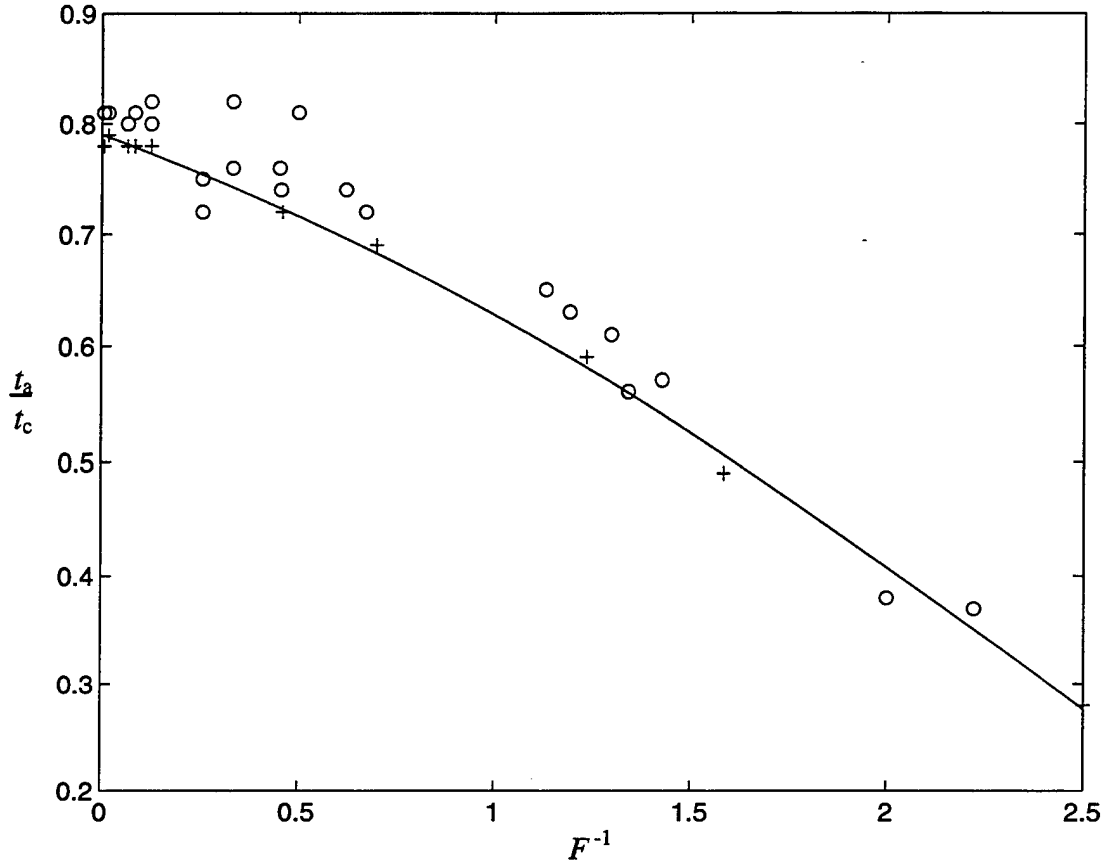

Figure 44. The ratio t_a/t_c for the limiting frontal cases (crosses) establishes a lower bound for that ratio. The solid line is a second order polynomial fit for these cases. Stronger frontogenetical cases (circles) tend to lie above the limit.

temperature gradient near the upper and lower boundaries change due to the divergent wind. The point of maximum gradient is initially located in the center of the imbalance region and shifts toward the warmer air as shown in Figure 29. The temperature field is modified in such a way that part of the temperature gradient becomes steeper and collapses into a front. The remaining part of the gradient becomes smoother. The analysis of all cases where frontogenesis occurred show no trend in the data. The average of the amount of temperature involved in the jump (normalized by $\Delta\theta$) is 0.175 with a standard

deviation of 0.045 (for a sample of 28 fronts). This amount does not seem to be changed for different parameters and characteristics. The variability is probably explained by the fact that model outputs are recorded at an interval $\Delta t = 0.09f^{-1}$. It means that the front may be formed at a different time than the recorded time. A source of error is the difficulty of determining where the jump starts and finishes. The criteria used here was the use of the largest changes in the slope of the temperature distribution.

The change in the position of maximum temperature gradient is also not constant for all frontal cases. The speed of the point of maximum temperature from the initial position until the jump forms is presented in Figure 45, as a function of *Ro*. The crosses

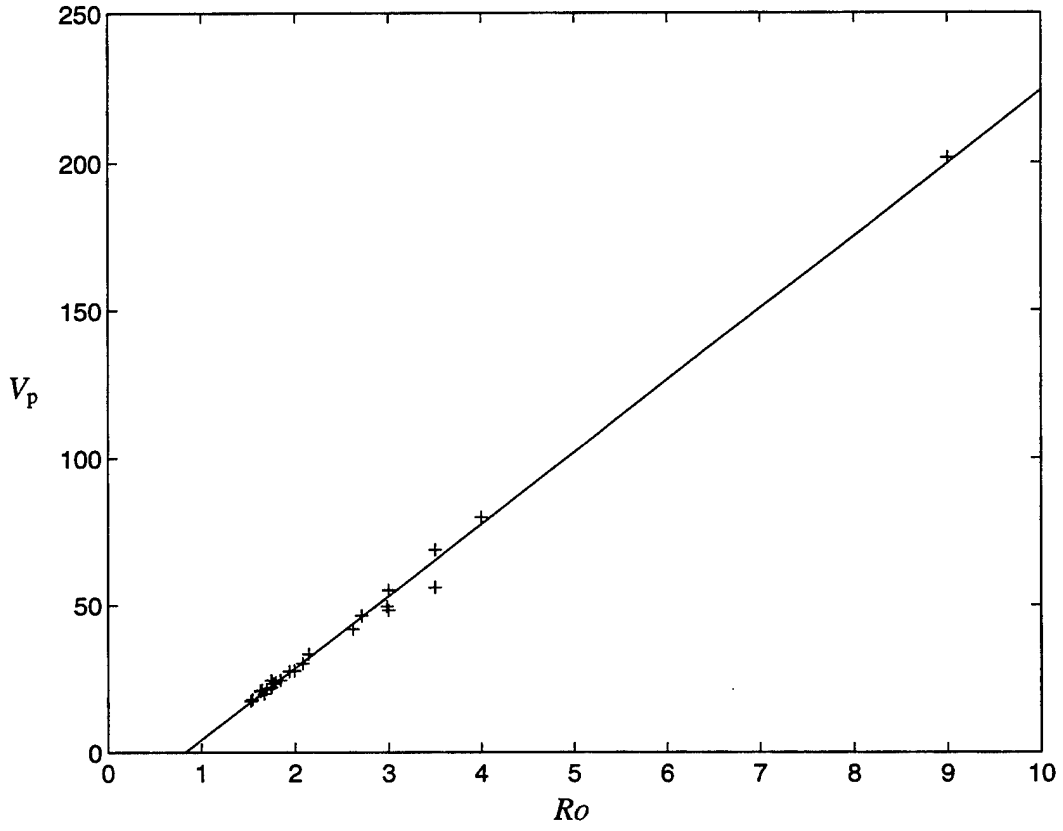

Figure 45. Speed of propagation (V_p) of the position of maximum temperature gradient for frontal cases (crosses) as a function of *Ro*. The solid line is the first order polynomial fit for the crosses.

represent the frontal cases in this work and the solid line is the first order polynomial fit for those points. The larger the Rossby number, the faster the movement of the temperature gradient. The speed is calculated using the change in the position of the d-value and the time for frontal formation (t_c).

VII. CONCLUSIONS

The numerical model of Williams et al. (1992) is used to study frontogenesis from unbalanced initial conditions. The dependent variables are assumed to be independent of y. The hydrostatic Boussinesq primitive equations are used with no diffusion of heat or momentum. The model is bounded at the top and bottom by rigid planes. Periodic boundary conditions are used in the horizontal. Stretching horizontal coordinates are used to give fine resolution in the region of frontal formation. The lateral boundaries are placed far enough from the imbalance region to avoid wave reflection. The initial temperature field has a constant vertical stratification.

The initial imbalance is obtained by allowing a horizontal temperature gradient to exist while the initial wind is zero. In a stably stratified atmosphere, gravity waves are excited and propagate away from the imbalance region, provided no reflection occurs at the lateral boundaries. Therefore, the atmosphere tends toward a geostrophic balance away from vertical boundaries. Near these boundaries, the temperature gradient oscillates or it collapses into a front, depending on the initial Rossby (Ro) and Froude (F) numbers.

A relationship between Ro and F is established to limit situations where a front may or may not form. Therefore, if the initial Ro and F of an imbalance region can be determined, the unbalanced contribution for future development of discontinuities can be estimated. This relationship also shows how intense the process is, depending on the distance of the point (Ro, F) from the limiting curve. The scale of the geostrophic adjustment far from the boundaries is likewise determined by Ro and F. Large scale adjustment happens when $F > Ro/\pi$ and the fluid adjusts to the initial mass field. The

adjustment depends on the initial momentum field when $F < Ro/\pi$, and the initial imbalance scale is small compared to L_R.

Large Ro and small F fluids are more divergent and less dependent on the inertial period, which leads to faster frontogenesis and more rapid geostrophic adjustment. A zero planetary vorticity ($Ro \rightarrow \infty$) case is compared to a large Ro flow with $f = 10^{-4}$ s^{-1} (the other parameters held constant), and the results show very subtle differences. The period of oscillation for the nonfrontal cases is inertial when $Ro < 1.53$, and depends on Ro, F, and N for larger Ro. The amount of temperature involved in the frontal zone is about 17 % of the temperature anomaly. This differs from the simple inviscid Burger's equation, where almost all the temperature collapses into a front.

For large F Blumen's curve is very close to the critical curve in our study, since his value for large F is $Ro = 1.45$. This is also shown by BW96 who are considering the zero potential vorticity case. In this case the critical value should be very close because the initial conditions are the same. The latter are the same because the initial state is not changed by geostrophic adjustment. The difference between the Blumen's curve and our curve for large F is caused by the barotropic pressure contribution which is not included in the analytic theory. As F decreases the Blumen's curve falls below and to the left of our curve. Although the Blumen's curve is based on a weaker initial temperature field (it is the same along the upper and lower boundaries) this does not seem to be important because his curve is still to the left of our curve. If this effect were more important it would require larger Ro and a larger F. Apparently the geostrophic adjustment in the numerical model brings the temperature close to the initial field used by Blumen.

The larger difference between the Blumen's curve and our curve in the lower part of the *Ro* - *F* diagram must be caused by the barotropic pressure gradient term.

LIST OF REFERENCES

Arakawa, A., and V. R. Lamb, 1977: Computational design of the basic dynamically processes of the UCLA general circulation model. *Methods in Computational Physics,* Vol. 17, Academic Press, 174-264.

Blumen, W., 1995: Personal notes.

Blumen, W., and R. T. Williams, 1996: Unbalance frontogenesis with zero potential vorticity. Unpublished.

Blumen, W., and R. Wu, 1994: Geostrophic adjustment: Frontogenesis and energy conversion. *J. Phys. Oceanogr.*, **25**, 428-438.

Haltiner, G. J., and R. T. Williams, 1980: *Numerical prediction and dynamic meteorology*, John Wiley and Sons, 477 pp.

Hoskins, B. J., and F. P. Bretherton, 1972: Atmospheric frontogenesis models: Mathematical formulation and solution. *J. Atmos. Sci.*, **29**, 11-37.

Kay, A., 1992: Frontogenesis in gravity-driven flows with non-uniform density gradients. *J. Fluid Mech.*, **235**, 529-556.

Keyser, D., and R. A. Anthes, 1982: The influence of planetary boundary layer physics on frontal structure in the Hoskins-Bretherton horizontal shear model. *J. Atmos. Sci.*, **39**, 1783-1802.

Lorenz, E. N., 1960: Energy and numerical weather prediction. *Tellus*, **12**, 364-373.

Ogura, Y., and N. A. Phillips, 1962: Scale analysis of deep and shallow convection in the atmosphere. *J. Atmos. Sci.*, **19**, 173-179.

Simpson, J. E., and P. F. Linden, 1989: Frontogenesis in a fluid with horizontal density gradients. *J. Fluid Mech.*, **202**, 1-16.

Stone, P. H., 1966: Frontogenesis by horizontal wind deformation fields. *J. Atmos. Sci.*, **23**, 455-465.

Williams, R. T., 1967: Atmospheric frontogenesis: A numerical experiment. *J. Atmos. Sci.*, **24**, 627-641.

___, 1972: Quasi-geostrophic versus non-geostrophic frontogenesis. *J. Atmos. Sci.*, **29**, 3-10.

___, 1974: Numerical simulation of steady-state fronts. *J. Atmos. Sci.*, **31**, 1286-1296.

___, and R. P. Kurth, 1976: Formation of discontinuities in a stratified rotating atmosphere. *J. Geophys. Res.*, **81**, 1133-1140.

___, M. S. Peng, and D. A. Zankofski, 1992: Effects of topography on fronts. *J. Atmos. Sci.*, **49**, 287-305.

INITIAL DISTRIBUTION LIST

No. Copies

1. Defense Technical Information Center 2
   8725 John J. Kingman Rd., STE 0944
   Ft. Belvoir, VA 22060-6218

2. Dudley Knox Library 2
   Naval Postgraduate School
   411 Dyer Rd.
   Monterey, CA 93943-5101

3. Chairman, Code MR 1
   Meteorology Department
   Naval Postgraduate School
   Monterey, CA 93943

4. Prof. R. T. Williams, Code MR/Wu 3
   Meteorology Department
   Naval Postgraduate School
   Monterey, CA 93943

5. Prof. M. S. Peng, Code MR/Pg 2
   Meteorology Department
   Naval Postgraduate School
   Monterey, CA 93943

6. LCDR A. P. C. Neves 2
   Av. Alda Garrido, 341/103
   Rio de Janeiro - RJ 22621-000
   Brazil

7. Diretoria de Hidrografia e Navegacao 3
   c/o Brazilian Naval Commission
   4706 Wisconsin Ave., NW
   Washington, D.C. 20016

8. Prof. W. Blumen 1
   Campus Box 391
   University of Colorado
   Boulder, CO 80309